Analytical solution of a gradient-enhanced damage model for quasi-brittle failure

Analytical solution of a gradient-enhanced damage model for quasi-brittle failure

Liang Xue[a], Xiaodan Ren*[a] and Francesco Freddi[b]

[a]College of Civil Engineering, Tongji University, 1239 Siping Road, Shanghai, 200092, P.R.China
[b]Departmend of Engineering and Architecture, Università degli Studi di Parma, Parco Area delle Scienze 181/A, Parma, 43124, Italy

ARTICLE INFO

Keywords:
Non-local model
Damage model
Gradient-enhanced damage model
Fracture mechanics
Analytical solution

ABSTRACT

This paper presents an approach for analytically solving gradient-enhanced damage (GED) models. The proposed approach provides rigorous proofs for essential phenomena observed in the traditional GED model, including damage widening, characteristic length sensitivity, and stress-locking. The derived cohesive law is a useful technique for accurately determining the material parameters of the GED model, significantly reducing the sensitivity to characteristic length. Furthermore, this study presents an isotropic damage model that considers both tensile and shear failures and can capture complex crack paths. Finally, a series of numerical examples is shown to demonstrate the efficacy of the suggested method.

1. Introduction

Quasi-brittle materials are commonly used in structural engineering, where fracture is the most typical failure mode. How to predict the failure of structures and the rupture process of quasi-brittle materials is an essential constraint in structural design [1]. Non-linear finite element analysis combined with damage theory provides a valuable tool for analyzing and designing engineering structures. Non-linear finite element analysis can predict the deformation of structures under large deformations and complex loading situations, while damage models can describe the non-linear behavior of quasi-brittle materials during stressing [2, 3, 4]. However, strain softening in quasi-brittle materials will result in a negative tangential modulus [5, 6], ellipticity loss of the formulation [7, 8, 9, 10]. As a result, the differential equations become ill-posed [11, 12, 13], leading to

xltj@tongji.edu.cn (L. Xue); rxdtj@tongji.edu.cn (X. Ren*); francesco.freddi@unipr.it (F. Freddi)
http://www.renxiaodan.com (X. Ren*)
ORCID(s):

numerical results that are dependent on mesh size and shape for conventional damage models in finite element analysis.

To address the issue of strain softening and ill-posedness in finite element analysis of quasi-brittle materials, several advanced modeling techniques have been developed in recent years. These techniques include non-local approaches [14, 15, 12, 16, 17], regularization methods [18, 19, 20], and phase-field models [21, 22, 23, 24, 25, 26]. These approaches incorporate the effect of non-local interactions into the constitutive model, which enables the strain localization to occur over a finite length scale. This length scale can be related to the characteristic material length, such as the aggregate size in concrete. Non-local models can overcome the ill-posedness issue and produce physically meaningful solutions that are mesh-independent. A regularization term is introduce into the constitutive model, which smooths out the strain softening behavior and eliminates the negative tangential modulus. Phase-field models describe the damage process as a diffuse interface between the intact and damaged regions. The damage evolution is governed by a phase-field variable that varies smoothly across the interface. Phase-field models can capture complex fracture patterns, such as branching and merging, and provide a unified framework for modeling crack initiation and propagation. Overall, these advanced modeling techniques have greatly improved the accuracy and reliability of finite element analysis for quasi-brittle materials [27].

The strain softening of quasi-brittle materials is mainly due to the interaction and growth of microcracks. Therefore, the material's fracture depends not only on the local stress state; but also on the non-local effects of the material's microstructure [13]. The general classical non-local models can be divided into two categories: the non-local integral approach [11, 27] and the gradient-enhanced model [12]. The non-local integral approach integrates local variables over a certain neighborhood to consider the effects of long-range interactions between material points. In the case of quasi-brittle materials, this neighbourhood can be defined in terms of the distance between material points. The non-local integral approach is relatively simple to implement numerically, but it does require reworking the code for finite element solutions.

On the other hand, the Gradient-Enhanced Damage (GED) model [12] is a more sophisticated approach to modeling non-local behavior in quasi-brittle materials. The gradient-enhanced damage model incorporates the spatial gradients of the damage variables into the governing equations of the damage evolution, and by choosing a suitable internal length, it allows for the consideration of non-local interactions within the neighbourhood of the material point [13, 15]. To solve the GED models, Taylor series expansions can be used to obtain the Poisson/Helmholtz equations required to describe the gradient effects. Finite elements can then be used to solve these equations by discretizing the elements, constructing shape functions for the non-local variables, and introducing additional degrees of freedom at each element node. This allows the non-local variables to be solved as an unknown quantity with the displacement degrees of freedom. One advantage of the GED models over the non-local integral approach is that it can be easily embedded in generic finite element software using the UEL and UMAT subroutines [28]. Additionally, the GED models allow for a more accurate description of the damage behavior of the material as a gradient field [29], which can lead to more accurate predictions of material behavior under different loading conditions. The GED models have been used in various applications, including analyzing structures subjected to dynamic loading, predicting material failure under various loading conditions, and developing new materials with improved mechanical properties. However, the GED model suffers from damage-widening [30, 31], characteristic length sensitivity [26], and stress-locking effects [32, 33, 34], which limit its application in structural failure prediction.

In summary, non-local damage models have critical applications in the fields of materials science, mechanics, and engineering [35, 14, 25, 36, 37]. They can help researchers and engineers better understand and predict the damage and destructive behavior of materials, informing the design of materials and the safety assessment of engineering structures. However, most non-local damage models are empirical and lack the basis for analytical solutions mathematically, which causes many problems, such as damage-widening, characteristic length sensitivity, and stress locking. Therefore, studying the analytical solution of non-local damage models is of great significance [38]. Peerlings et al. [12] provide an analytical solution to the GED model, but the

method can only solve the ideal elastic-plastic model rather than the strain-softened damage model. Lorentz [39] demonstrate that the non-local constitutive equations are consistent with the cohesive law under some conditions. Bisconti et al. [40] prove the existence and uniqueness of weak solutions under conditions of progressive damage. Zhao and Cheng [41] provides a global weak solution to the 1D phase-field model with inhomogeneous elasticity. Although the analytical solution of non-local damage models has gradually attracted the attention of researchers, there is still a lack of a standard mathematical method to solve the GED model. Therefore, this paper proposes a method to solve the GED model analytically and mathematically and prove damage-widening [30, 31], characteristic length sensitivity [26], and stress-locking phenomena [32, 33, 34].

This paper is organized as follows: Section 2 gives the analytical solutions of the gradient damage model for three different nonlocal variables, solving for their damage profiles and cohesive laws. Section 4 presents an isotropic damage model that is both simple and practical. Section 5 presents several numerical examples that demonstrate the accuracy of the analytical solution in the proposed method, the reduction of sensitivity to characteristic length through material parameter calibration using the proposed method, and the ability to capture crack paths under complex loading conditions. Section 6 concludes this paper. Interested readers can download the code for this study from : https://github.com/XLiang123/Gradient-enhanced-damage-model

2. Analytical solutions for GED models

In order to compare the similarities and differences between various non-local damage models, a simple one-dimensional uniaxial tensile test is used to calculate the analytical solution of the gradient-enhanced damage model.

Assume a bar $x \in \left[-L/2, L/2\right]$ sufficiently long such that crack evolution is not affected by boundary effects. The bar is loaded at both ends by increasing displacements u^* along opposite directions (Fig. 1). Body forces b^* are neglected. For simplicity, it is assumed that the crack is initiated at the symmetric point $x = 0$ and the localization band is lumped in the domain

$[-D/2, D/2]$, with $D < L$ being the half bandwidth not necessarily constant. The material parameters employed in the analytical solution are detailed in Section 5.

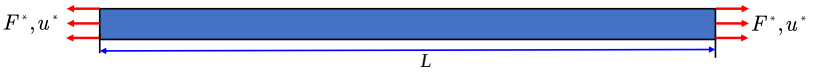

Figure 1: Uniaxial traction of a softening bar: geometry, loading and boundary conditions

2.1. Nonlocal equivalent strain energy model

When the driving force for the evolution of non-local damage is the strain energy Y, the differential equation for the non-local model is as follows:

$$\begin{cases} l_c^2 \nabla^2 \bar{Y} - \bar{Y} + Y = 0 & \text{(1a)} \\ Y = \dfrac{1}{2}\, \boldsymbol{\varepsilon} : \mathbb{E} : \boldsymbol{\varepsilon} & \text{(1b)} \end{cases}$$

where Y is the local strain energy; $\bar{Y}$ is the non-local strain energy; l_c is the characteristic length; $\boldsymbol{\varepsilon}$ is a second-order strain tensor, and $\mathbb{E}$ is a fourth-order isotropic linear elastic stiffness tensor. In the case of Poisson's ratio $\nu < 0.5$ and uniaxial tensile, Eq. (1) can be rewritten as:

$$\begin{cases} l_c^2 \dfrac{\mathrm{d}^2 \bar{Y}}{\mathrm{d}x^2} - \bar{Y} + Y = 0 & \text{(2a)} \\ Y = \dfrac{1}{2} E_0 \varepsilon^2 & \text{(2b)} \end{cases}$$

where E_0 is Young's modulus; ε is the uniaxial strain.

In GED model, the softening law can be naturally embedded into the non-local model via $\bar{\phi} = \bar{\phi}\left(\bar{Y}\right)$, where $\bar{\phi}\left(\bar{Y}\right)$ is the softening function [1] in the general form. For the purpose of simplicity, we consider the soften function in the following form as an example. As we can see:

$$\bar{\phi} = \bar{\phi}(\bar{Y}) = \begin{cases} 1 - \dfrac{f_{\mathrm{t}}}{E_0\sqrt{\dfrac{2\bar{Y}}{E_0}}} e^{\alpha\left(1-\frac{\sqrt{\frac{2\bar{Y}}{E_0}}}{\varepsilon_{\mathrm{c}}}\right)} & \bar{Y} \geq \bar{Y}_{\mathrm{c}} \quad (3a) \\ 0 & \text{Otherwise} \quad (3b) \end{cases}$$

where f_{t} is the tensile strength; $\varepsilon_{\mathrm{c}} = f_{\mathrm{t}}/E_0$ is the strain corresponding to the peak stress; $\bar{Y}_{\mathrm{c}} = \frac{f_{\mathrm{t}}^2}{2E_0}$; and α is the parameter controlling the softening behavior. Here the strength is considered as an exponential softening, and in a later paper, we will provide different softening laws.

According to the classical damage theory [see, 2, 3, 4, 42, and so on.], the relation between stress and strain is commonly expressed as follows:

$$\sigma = \left(1 - \bar{\phi}\right) E_0 \varepsilon \tag{4}$$

Combining Eq. (2b), Eq. (3a) and Eq. (4), we can obtain:

$$Y = \frac{\sigma^2}{{f_t}^2} \bar{Y} e^{-2\alpha\left(1-\frac{\sqrt{\frac{2\bar{Y}}{E_0}}}{\varepsilon_c}\right)} \tag{5}$$

By substituting Eq. (5) into Eq. (2a), one obtains

$$l_c^2 \frac{\mathrm{d}^2\bar{Y}}{\mathrm{d}x^2} - \bar{Y} + \frac{\sigma^2\bar{Y}}{{f_t}^2} e^{-2\alpha\left(1-\frac{\sqrt{\frac{2\bar{Y}}{E_0}}}{\varepsilon_c}\right)} = 0 \tag{6}$$

Then multiplying Eq. (6) by $\frac{\mathrm{d}\bar{Y}}{\mathrm{d}x}$ and integrating with respect to x, we have

$$\frac{l_c^2}{2}\left(\frac{\mathrm{d}\bar{Y}}{\mathrm{d}x}\right)^2 - \frac{1}{2}\bar{Y}^2 + \frac{2e^{-2\alpha}\sigma^2}{{f_t}^2\mathrm{B}^4}\left(\mathrm{B}^3\bar{Y}^{\frac{3}{2}} - 3\mathrm{B}^2\bar{Y} + 6\mathrm{B}\sqrt{\bar{Y}} - 6\right)e^{\mathrm{B}\sqrt{\bar{Y}}} = \mathrm{A} \tag{7}$$

where A is the integration constant; and another constant $\mathrm{B} = 2\sqrt{2}\alpha / \left(\varepsilon_c \sqrt{E_0}\right)$. Let $\bar{Y}^*$ denote the value of $\bar{Y}$ at the location of x^* where the damage reaches the maximum value. By introducing the boundary conditions $\nabla\bar{Y}(x) = 0$ $(\forall x \in \partial\Omega_{\bar{Y}^*})$ and the continuation condition $\nabla\bar{Y}(x^*) = 0$, we resolve the integration constant A as follows:

$$\mathrm{A} = \frac{\left(\bar{Y}^*\right)^2 f\left(\bar{Y}_\mathrm{c}\right) - \left(\bar{Y}_\mathrm{c}\right)^2 f\left(\bar{Y}^*\right)}{2\left(f\left(\bar{Y}^*\right) - f\left(\bar{Y}_\mathrm{c}\right)\right)} \tag{8}$$

where $\bar{Y}^*$ is the value of $\bar{Y}$ at x^*; and the function $f(\cdot)$ as follows:

$$\begin{cases} f\left(\bar{Y}_\mathrm{c}\right) = \left[\mathrm{B}^3\left(\bar{Y}_\mathrm{c}\right)^{\frac{3}{2}} - 3\mathrm{B}^2\bar{Y}_\mathrm{c} + 6\mathrm{B}\sqrt{\bar{Y}_\mathrm{c}} - 6\right] e^{\mathrm{B}\sqrt{\bar{Y}_\mathrm{c}}} & \text{(9a)} \\ f\left(\bar{Y}^*\right) = \left[\mathrm{B}^3\left(\bar{Y}^*\right)^{\frac{3}{2}} - 3\mathrm{B}^2\bar{Y}^* + 6\mathrm{B}\sqrt{\bar{Y}^*} - 6\right] e^{\mathrm{B}\sqrt{\bar{Y}^*}} & \text{(9b)} \end{cases}$$

According to Eq. (7), $\frac{\mathrm{d}x}{\mathrm{d}\bar{Y}}$ can be easily derived in the following form:

$$\frac{\mathrm{d}x}{\mathrm{d}\bar{Y}} = \frac{l_\mathrm{c}}{\sqrt{2\mathrm{A} + \bar{Y}^2 - \frac{4e^{-2\alpha}\sigma^2}{{f_\mathrm{t}}^2\mathrm{B}^4}(\mathrm{B}^3\bar{Y}^{\frac{3}{2}} - 3\mathrm{B}^2\bar{Y} + 6\mathrm{B}\sqrt{\bar{Y}} - 6)e^{\mathrm{B}\sqrt{\bar{Y}}}}} \tag{10}$$

By integrating both sides of Eq. (10) with respect to $\mathrm{d}\bar{Y}$, one obtains:

$$x = \pm\int_{\bar{Y}}^{\bar{Y}^*} \frac{l_\mathrm{c}}{\sqrt{2\mathrm{A} + \bar{Y}^2 - \frac{4e^{-2\alpha}\sigma^2}{{f_\mathrm{t}}^2\mathrm{B}^4}(\mathrm{B}^3\bar{Y}^{\frac{3}{2}} - 3\mathrm{B}^2\bar{Y} + 6\mathrm{B}\sqrt{\bar{Y}} - 6)e^{\mathrm{B}\sqrt{\bar{Y}}}}} \mathrm{d}\bar{Y} \tag{11}$$

The profile of $\bar{Y}$can be solved numerically according to Eq. (11). Fig. 2 shows the profiles of $\bar{Y}$ at different stages of $\bar{Y}^*$.

The profiles of damage along the rod at different loading stages are presented in Fig. 3. It can be clearly observed that the bandwidth of the damage region expands when the loading increases. This is the so-called damage widening/broadening mentioned in classic works [30, 31].

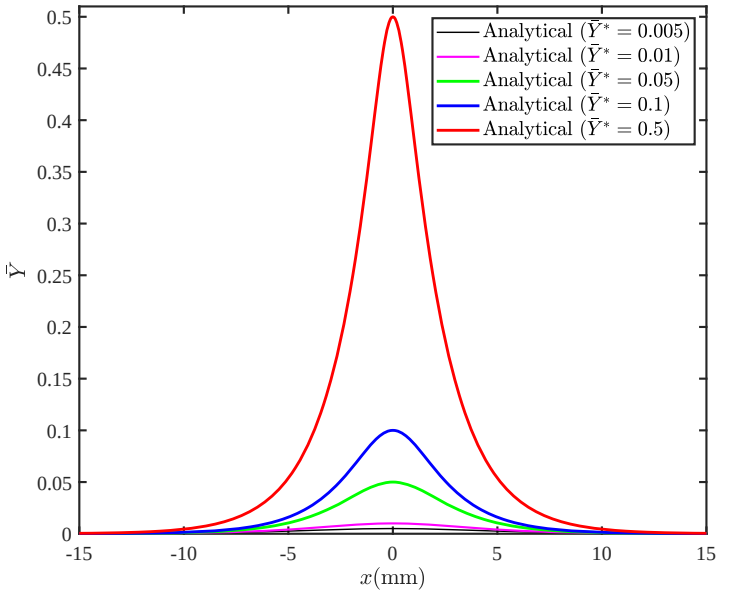

Figure 2: Profiles of the non-local model strain energy $\bar{Y}$

In addition, when the damage has evolved to a certain stage, unloading will occur at the edges of the regularization region.

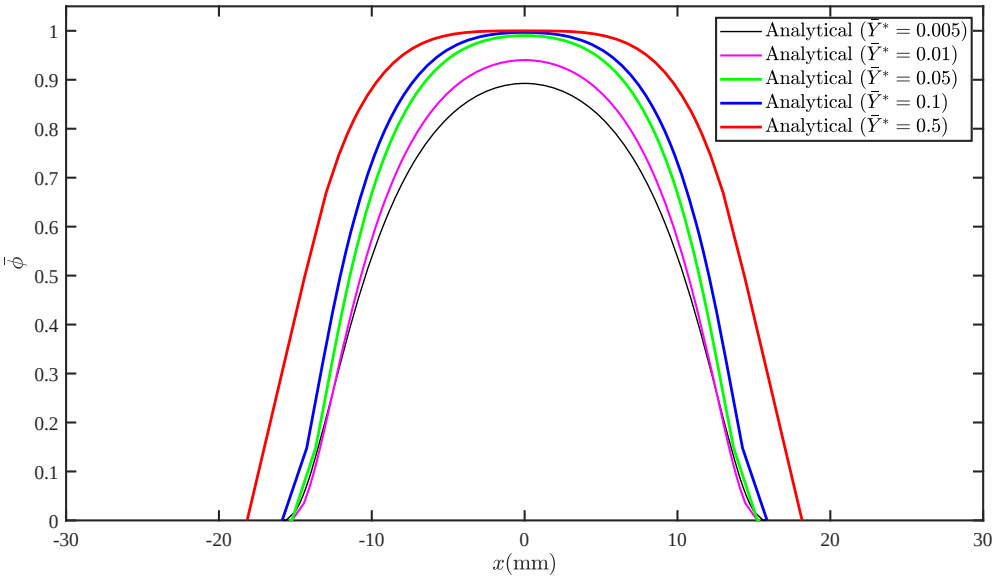

Figure 3: Non-local model damage profiles

The stress over the 1D bar and the traction σ in the underlying cracking zone can be evaluated at x^* using Eq. (7). According to the continuation condition $\nabla\bar{Y}\left(x^*\right)=0$ and Eq. (7), the stress σ on a one-dimensional rod can be expressed as:

$$\sigma=\sqrt{\left(\mathrm{A}+\frac{1}{2}\left(\bar{Y}^*\right)^2\right)\frac{{f_\mathrm{t}}^2\mathrm{B}^4}{(\mathrm{B}^3\left(\bar{Y}^*\right)^{\frac{3}{2}}-3\mathrm{B}^2\bar{Y}^*+6\mathrm{B}\sqrt{\bar{Y}^*}-6)e^{\mathrm{B}\sqrt{\bar{Y}^*}}}\frac{e^{2\alpha}}{2}} \tag{12}$$

The total displacement u^* at the bar end can be calculated by using the integration as follows:

$$u^*=\int_0^L\varepsilon\mathrm{d}x=\int_0^L\frac{\sigma}{\left(1-\bar{\phi}\right)E_0}\mathrm{d}x=\frac{\sigma L}{E_0}+\delta_\mathrm{n}\left(\sigma,\bar{Y}^*\right) \tag{13}$$

On the right-hand side of Eq.(13), the first term is the elastic displacement of the whole rod and the second term is the width of the crack. Substituting Eq. (10) into Eq.(13), one obtains the nonlinear displacement component as follows:

$$\begin{aligned}\delta_\mathrm{n}\left(\sigma,\bar{Y}^*\right)&=\int_{\Omega_{\bar{Y}^*}}\frac{\bar{\phi}\sigma}{\left(1-\bar{\phi}\right)E_0}\mathrm{d}x=2\int_0^{\bar{Y}^*}\frac{\bar{\phi}\left(\bar{Y}\right)\sigma}{\left(1-\bar{\phi}\left(\bar{Y}\right)\right)E_0}\frac{\mathrm{d}x}{\mathrm{d}\bar{Y}}\mathrm{d}\bar{Y}\\&=\frac{2l_\mathrm{c}}{E_0}\int_0^{\bar{Y}^*}\frac{\bar{\phi}\left(\bar{Y}\right)\sigma}{\left(1-\bar{\phi}\left(\bar{Y}\right)\right)\sqrt{2\mathrm{A}+\bar{Y}^2-\frac{4e^{-2\alpha}\sigma^2}{{f_\mathrm{t}}^2B^4}(B^3\bar{Y}^{\frac{3}{2}}-3B^2\bar{Y}+6B\sqrt{\bar{Y}}-6)e^{B\sqrt{\bar{Y}}}}}\mathrm{d}\bar{Y}\end{aligned} \tag{14}$$

As can be seen, Eq. (12) establishes the relation between $\bar{Y}^*$ and σ, while Eq. (14) establishes the relation between $\bar{Y}^*$ and δ_n. Therefore, the relation between σ and δ_n could be resolved by combining Eq. (12) and Eq. (14). The results can be found in Fig. 4. If the damage of a bar under uniaxial tension could be attributed to a mode I cohesive crack, the resolved $\sigma-\delta_\mathrm{n}$ relation could be considered as the corresponding cohesive law. By using analytically derived cohesive laws, the link between the material fracture energy $G_\mathrm{I}=\int\sigma\mathrm{d}\delta_\mathrm{n}$, the softening parameter α, and the characteristic length l_c can be established, which will alleviate the characteristic length sensitivity in the GED model.

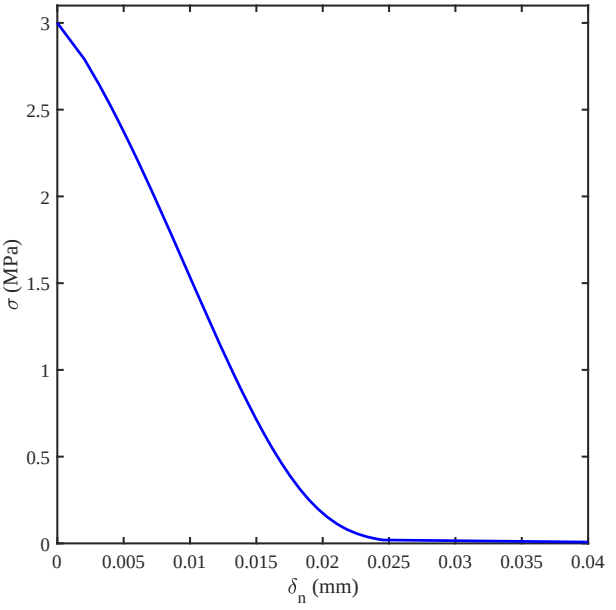

Figure 4: Cohesive law ($\delta_{\mathrm{n}} - \sigma$)

2.2. Nonlocal equivalent strain model

In this subsection, we consider the non-local damage driven by equivalent strain $\bar{\varepsilon}$. The differential form for the non-local model is expressed as follows:

$$l_{\mathrm{c}}^2 \nabla^2 \bar{\varepsilon} - \bar{\varepsilon} + \varepsilon = 0 \tag{15}$$

where $\bar{\varepsilon}$ is the non-local equivalent strain and ε is the local equivalent strain. In the case of one-dimensional uniaxial tension, Eq. (15) can be reduced to the following form:

$$l_{\mathrm{c}}^2 \frac{\mathrm{d}^2 \bar{\varepsilon}}{\mathrm{d}x^2} - \bar{\varepsilon} + \varepsilon = 0 \tag{16}$$

The relation between the non-local strain $\bar{\varepsilon}$ and the non-local damage $\bar{\phi}$ is needed for further development of the model. Here we adopt the exponentially softening form which is similar to Eq. (3). We have:

$$\bar{\phi} = \bar{\phi}(\bar{\varepsilon}) = \begin{cases} 1 - \dfrac{f_t}{E_0 \bar{\varepsilon}} e^{\alpha\left(1-\frac{\bar{\varepsilon}}{\varepsilon_c}\right)} & \bar{\varepsilon} \geq \varepsilon_c \quad (17a) \\ 0 & \text{Otherwise} \quad (17b) \end{cases}$$

Combining Eq. (4) with Eq. (17a), we can obtain

$$\varepsilon = \frac{\sigma}{f_t e^{\alpha}} \bar{\varepsilon} e^{\frac{\alpha}{\varepsilon_c}\bar{\varepsilon}} \tag{18}$$

By subsituting Eq. (18) into Eq. (16), one obtains

$$l_c^2 \frac{\mathrm{d}^2 \bar{\varepsilon}}{\mathrm{d}x^2} - \bar{\varepsilon} + \frac{\sigma}{f_t e^{\alpha}} \bar{\varepsilon} e^{\frac{\alpha}{\varepsilon_c}\bar{\varepsilon}} = 0 \tag{19}$$

Then multiplying Eq. (19) by $\frac{\mathrm{d}\bar{\varepsilon}}{\mathrm{d}x}$ and integrating with respect to x, we have

$$\frac{l_c^2}{2}\left(\frac{\mathrm{d}\bar{\varepsilon}}{\mathrm{d}x}\right)^2 - \frac{1}{2}\bar{\varepsilon}^2 + \frac{\sigma}{f_t e^{\alpha}} e^{\frac{\alpha}{\varepsilon_c}\bar{\varepsilon}} \left(\frac{\alpha}{\varepsilon_c}\bar{\varepsilon} - 1\right) \frac{{\varepsilon_c}^2}{\alpha^2} = \mathrm{A} \tag{20}$$

where A is the integration constant.

Let $\bar{\varepsilon}^*$ denote the value of $\bar{\varepsilon}$ at the point of maximum damage x^* along the rod during stretching. By introducing the boundary conditions $\nabla\bar{\varepsilon}(x) = 0$ $(\forall x \in \partial\Omega_{\bar{\varepsilon}^*})$ and the continuation condition $\nabla\bar{\varepsilon}(x^*) = 0$, we resolve the integration constant A as follows:

$$\mathrm{A} = \frac{\frac{\left(\bar{\varepsilon}_c\right)^2}{2e^{\alpha}(\alpha-1)} - \frac{(\bar{\varepsilon}^*)^2}{2e^{\frac{\alpha}{\varepsilon_c}\bar{\varepsilon}^*}\left(\frac{\alpha}{\varepsilon_c}\bar{\varepsilon}^*-1\right)}}{\frac{1}{e^{\frac{\alpha}{\varepsilon_c}\bar{\varepsilon}^*}\left(\frac{\alpha}{\varepsilon_c}\bar{\varepsilon}^*-1\right)} - \frac{1}{e^{\alpha}(\alpha-1)}} \tag{21}$$

According to Eq. (20), $\frac{\mathrm{d}x}{\mathrm{d}\bar{\varepsilon}}$ can be easily resolved in the following form:

$$\frac{\mathrm{d}x}{\mathrm{d}\bar{\varepsilon}} = \frac{l_c}{\sqrt{2\mathrm{A} + \bar{\varepsilon}^2 - \frac{2\sigma}{f_t e^{\alpha}} e^{\frac{\alpha}{\varepsilon_c}\bar{\varepsilon}} \left(\frac{\alpha}{\varepsilon_c}\bar{\varepsilon} - 1\right) \frac{{\varepsilon_c}^2}{\alpha^2}}} \tag{22}$$

By performing integration on both sides of Eq. (22), one obtains:

$$x = \pm \int_{\bar{\varepsilon}}^{\bar{\varepsilon}^*} \frac{l_c}{\sqrt{2A + \bar{\varepsilon}^2 - \frac{2\sigma}{f_t e^{\alpha}} e^{\frac{\alpha}{\varepsilon_c}\bar{\varepsilon}} \left(\frac{\alpha}{\varepsilon_c}\bar{\varepsilon} - 1\right) \frac{{\varepsilon_c}^2}{\alpha^2}}} d\bar{\varepsilon} \tag{23}$$

Based on Eq. (23), the profile of $\bar{\varepsilon}$ can be solved numerically. Fig. 5 gives the simulated profiles of $\bar{\varepsilon}$ at different stages of $\bar{\varepsilon}^*$. Moreover, the profiles of damage along the rod at different loading stages are presented in Fig. 6. Similar to the results shown in Fig. 3, the damage widening/broadening could be clearly observed. Furthermore, once the damage has progressed to a certain level, it unloads at the edges of the regularized region.

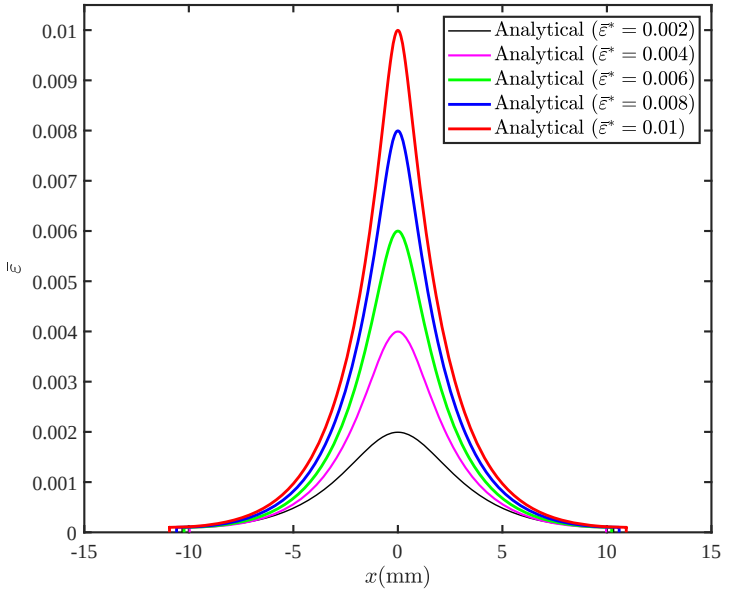

Figure 5: Profiles of the non-local model strain $\bar{\varepsilon}$

By using the continuation condition $\nabla\bar{\varepsilon}(x^*) = 0$ and Eq. (20), the stress σ over the rod can be resolved in the following form:

$$\sigma = \frac{f_t e^{\alpha} \alpha^2}{{\varepsilon_c}^2} \frac{1}{e^{\frac{\alpha}{\varepsilon_c}\bar{\varepsilon}^*} \left(\frac{\alpha}{\varepsilon_c}\bar{\varepsilon}^* - 1\right)} \left(A + \frac{1}{2}(\bar{\varepsilon}^*)^2\right) \tag{24}$$

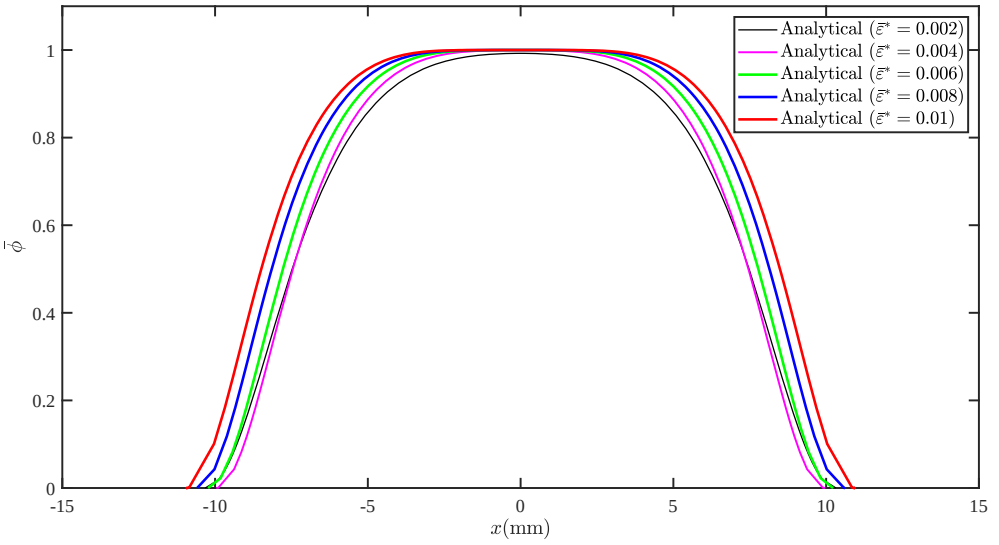

Figure 6: Non-local model damage profiles

The total displacement u^* at the bar end can be calculated by integrating strain field over the rod. We have

$$u^* = \int_0^L \varepsilon \mathrm{d}x = \int_0^L \frac{\sigma}{\left(1-\bar{\phi}\right) E_0} \mathrm{d}x = \frac{\sigma L}{E_0} + \delta_{\mathrm{n}}\left(\sigma, \bar{\varepsilon}^*\right) \tag{25}$$

On the right-hand side of Eq.(25), the first term is the elastic deformation of the whole rod and the second term is the inelastic deformation. Substituting Eq. (22) into Eq.(25), one obtains the inelastic defromation component as follows:

$$\begin{aligned} \delta_{\mathrm{n}}\left(\sigma, \bar{\varepsilon}^*\right) &= \int_{\Omega_{\bar{\varepsilon}^*}} \frac{\bar{\phi}\sigma}{\left(1-\bar{\phi}\right) E_0} \mathrm{d}x = 2\int_0^{\bar{\varepsilon}^*} \frac{\bar{\phi}\left(\bar{\varepsilon}\right)\sigma}{\left(1-\bar{\phi}\left(\bar{\varepsilon}\right)\right) E_0} \frac{\mathrm{d}x}{\mathrm{d}\bar{\varepsilon}} \mathrm{d}\bar{\varepsilon} \\ &= \frac{2l_{\mathrm{c}}}{E_0} \int_0^{\bar{\varepsilon}^*} \frac{\bar{\phi}\left(\bar{\varepsilon}\right)\sigma}{\left(1-\bar{\phi}\left(\bar{\varepsilon}\right)\right) \sqrt{2\mathrm{A} + \bar{\varepsilon}^2 - \frac{2\sigma}{f_{\mathrm{t}} e^{\alpha}} e^{\frac{\alpha}{\varepsilon_{\mathrm{c}}}\bar{\varepsilon}} \left(\frac{\alpha}{\varepsilon_{\mathrm{c}}}\bar{\varepsilon} - 1\right) \frac{{\varepsilon_{\mathrm{c}}}^2}{\alpha^2}}} \mathrm{d}\bar{\varepsilon} \end{aligned} \tag{26}$$

The cohesive law in the form of the relation between σ and δ_{n} could be resolved by combining Eq. (24) and Eq. (26). The results can be found in Fig. 7.

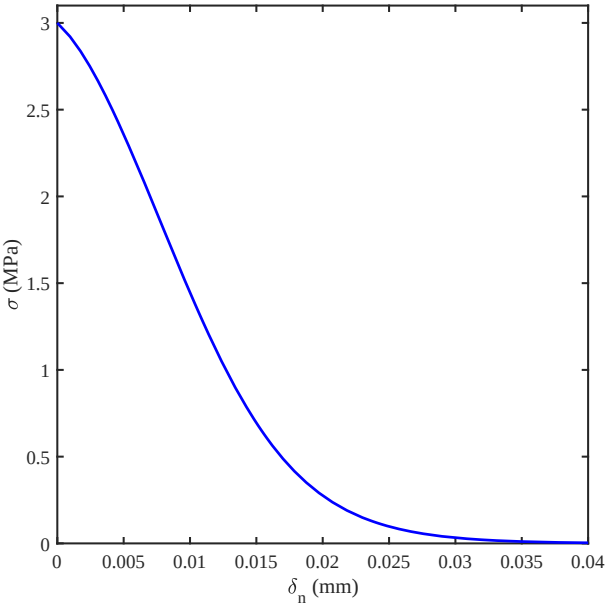

Figure 7: Cohesive law ($\delta_{\mathrm{n}} - \sigma$)

2.3. Nonlocal damage model

Finally, we discuss the gradient-enhanced model directly defined on the damage variable, which is in the following form:

$$l_{\mathrm{c}}^2 \nabla^2 \bar{\phi} - \bar{\phi} + \phi = 0 \tag{27}$$

where $\bar{\phi}$ is the non-local damage variable and ϕ is the local damage variable. For the 1-D case, Eq. (27) is reduced to the following form:

$$l_{\mathrm{c}}^2 \frac{\mathrm{d}^2 \bar{\phi}}{\mathrm{d}x^2} - \bar{\phi} + \phi = 0 \tag{28}$$

For simplicity, the soften funlction in the form of linear softening is adopted. One obtains

$$\phi = \begin{cases} 1 - \dfrac{f_{\mathrm{t}}}{E_0 \varepsilon} \dfrac{\varepsilon_{\mathrm{u}} - \varepsilon}{\varepsilon_{\mathrm{u}} - \varepsilon_{\mathrm{c}}} & \varepsilon \geq \varepsilon_{\mathrm{c}} \quad (29a) \\ 0 & \text{Otherwise} \quad (29b) \end{cases}$$

where ε_u is the ultimate strain at which the stress approaches zero. In the classical damage model, the relationship between stress and strain is commonly expressed as follows:

$$\sigma = \left(1 - \bar{\phi}\right) E_0 \varepsilon \tag{30}$$

Combining Eq. (29a) with Eq. (30), we can obtain:

$$\phi = 1 + \frac{f_\mathrm{t}}{E_0\left(\varepsilon_\mathrm{u} - \varepsilon_\mathrm{c}\right)} - \frac{f_\mathrm{t}\varepsilon_\mathrm{u}}{\left(\varepsilon_\mathrm{u} - \varepsilon_\mathrm{c}\right)} \frac{\left(1 - \bar{\phi}\right)}{\sigma} \tag{31}$$

By substituting Eq. (31) into Eq. (28), one obtains

$$l_\mathrm{c}^2 \frac{\mathrm{d}^2\bar{\phi}}{\mathrm{d}x^2} - \bar{\phi} + 1 + \frac{f_\mathrm{t}}{E_0\left(\varepsilon_\mathrm{u} - \varepsilon_\mathrm{c}\right)} - \frac{f_\mathrm{t}\varepsilon_\mathrm{u}}{\left(\varepsilon_\mathrm{u} - \varepsilon_\mathrm{c}\right)} \frac{\left(1 - \bar{\phi}\right)}{\sigma} = 0 \tag{32}$$

Then multiplying Eq. (32) by $\frac{\mathrm{d}\bar{\phi}}{\mathrm{d}x}$ and integrating with respect to x, we have

$$\frac{l_\mathrm{c}^2}{2}\left(\frac{\mathrm{d}\bar{\phi}}{\mathrm{d}x}\right)^2 - \frac{1}{2}\bar{\phi}^2 + \left(1 + \frac{f_\mathrm{t}}{E_0\left(\varepsilon_\mathrm{u} - \varepsilon_\mathrm{c}\right)}\right)\bar{\phi} + \frac{f_\mathrm{t}\varepsilon_\mathrm{u}}{2\left(\varepsilon_\mathrm{u} - \varepsilon_\mathrm{c}\right)\sigma}\left(1 - \bar{\phi}\right)^2 = \mathrm{A} \tag{33}$$

where A is the integration constant. Let $\bar{\phi}^*$ denote the value of $\bar{\phi}$ at the location of x^* where the damage reaches the maximum value. By introducing the boundary conditions $\bar{\phi}(x) = \nabla\bar{\phi}(x) = 0(\forall x \in \partial\Omega_{\bar{\phi}^*})$ and $\nabla\bar{\phi}(x^*) = 0$, we resolve the integration constant A as follows:

$$\mathrm{A} = \left[\frac{1}{2}\left(\bar{\phi}^*\right)^2 - \left(1 + \frac{f_\mathrm{t}}{E_0\left(\varepsilon_\mathrm{u} - \varepsilon_\mathrm{c}\right)}\right)\bar{\phi}^*\right] \frac{1}{\left[\left(1 - \bar{\phi}^*\right)^2 - 1\right]} \tag{34}$$

where $\bar{\phi}^*$ is the value of $\bar{\phi}$ at x^*.

According to Eq. (33), $\frac{\mathrm{d}x}{\mathrm{d}\bar{\phi}}$ can be easily derived in the following form:

$$\frac{\mathrm{d}x}{\mathrm{d}\bar{\phi}} = \frac{l_\mathrm{c}}{\sqrt{2\mathrm{A} + \bar{\phi}^2 - 2\left(1 + \frac{f_\mathrm{t}}{E_0(\varepsilon_\mathrm{u}-\varepsilon_\mathrm{c})}\right)\bar{\phi} - \frac{f_\mathrm{t}\varepsilon_\mathrm{u}}{(\varepsilon_\mathrm{u}-\varepsilon_\mathrm{c})\sigma}\left(1-\bar{\phi}\right)^2}} \tag{35}$$

By integrating both sides of Eq. (35) with respect to $\mathrm{d}\bar{\phi}$, one obtains:

$$x = \pm \int_{\bar{\phi}}^{\bar{\phi}^*} \frac{l_\mathrm{c}}{\sqrt{2\mathrm{A} + \bar{\phi}^2 - 2\left(1 + \frac{f_\mathrm{t}}{E_0(\varepsilon_\mathrm{u}-\varepsilon_\mathrm{c})}\right)\bar{\phi} - \frac{f_\mathrm{t}\varepsilon_\mathrm{u}}{(\varepsilon_\mathrm{u}-\varepsilon_\mathrm{c})\sigma}\left(1-\bar{\phi}\right)^2}} \mathrm{d}\bar{\phi} \tag{36}$$

The profile of $\bar{\phi}^*$ can be solved numerically based Eq. (36). The simulated profiles of $\bar{\phi}$ at different stages of $\bar{\phi}^*$ are shown in Fig. 8.

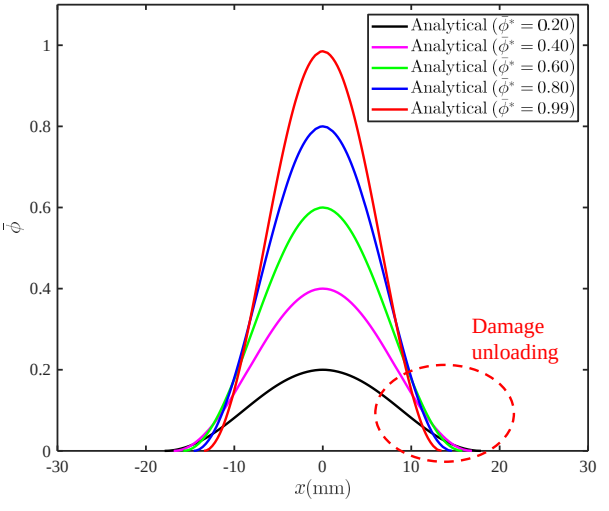

Figure 8: Non-local model damage profiles

As can be seen in Fig. 8, the bandwidths of the damage profile remain stable at different stages. The damage widening/broadening is suppressed in this case. However, one can observe that damage unloading takes place within the regularized crack band (pay attention to the ranges $[10, 20]$ and $[-20, -10]$ in Fig. 8) when the load increases. Thus this model may undergo instability for the simulation of structures [43, 44].

By introducing the boundary conditions $\nabla\bar{\phi}\left(x^{*}\right)=0$ into Eq. (33), the stress σ can be resolved as:

$$\sigma=\frac{f_{\mathrm{t}}\varepsilon_{\mathrm{u}}}{2\left(\varepsilon_{\mathrm{u}}-\varepsilon_{\mathrm{c}}\right)}\frac{\left(1-\bar{\phi}^{*}\right)^{2}}{\mathrm{A}+\frac{1}{2}\left(\bar{\phi}^{*}\right)^{2}-\left(1+\frac{f_{\mathrm{t}}}{E_{0}\left(\varepsilon_{\mathrm{u}}-\varepsilon_{\mathrm{c}}\right)}\right)\bar{\phi}^{*}} \tag{37}$$

Furthermore, the total displacement u^{*} at the bar end can be calculated by using the integration as follows

$$u^{*}=\int_{0}^{L}\varepsilon\mathrm{d}x=\int_{0}^{L}\frac{\sigma}{(1-\phi)E_{0}}\mathrm{d}x=\frac{\sigma L}{E_{0}}+\delta_{\mathrm{n}}\left(\sigma,\bar{\phi}^{*}\right) \tag{38}$$

On the right-hand side of Eq.(38), the first term is the elastic deformation of the whole rod and the second term is the inelastic deformation. Substituting Eq. (35) into Eq.(38), one obtains:

$$\begin{aligned}\delta_{\mathrm{n}}\left(\sigma,\bar{\phi}^{*}\right)&=\int_{\Omega_{\bar{\phi}^{*}}}\frac{\bar{\phi}\sigma}{\left(1-\bar{\phi}\right)E_{0}}\mathrm{d}x=2\int_{0}^{\bar{\phi}^{*}}\frac{\bar{\phi}\sigma}{\left(1-\bar{\phi}\right)E_{0}}\frac{\mathrm{d}x}{\mathrm{d}\bar{\phi}}\mathrm{d}\bar{\phi}\\&=\frac{2l_{\mathrm{c}}}{E_{0}}\int_{0}^{\bar{\phi}^{*}}\frac{\bar{\phi}\sigma}{\left(1-\bar{\phi}\right)\sqrt{2\mathrm{A}+\bar{\phi}^{2}-2\left(1+\frac{f_{\mathrm{t}}}{E_{0}\left(\varepsilon_{\mathrm{u}}-\varepsilon_{\mathrm{c}}\right)}\right)\bar{\phi}-\frac{f_{\mathrm{t}}\varepsilon_{\mathrm{u}}}{\left(\varepsilon_{\mathrm{u}}-\varepsilon_{\mathrm{c}}\right)\sigma}\left(1-\bar{\phi}\right)^{2}}}\mathrm{d}\bar{\phi}\end{aligned} \tag{39}$$

The cohesive law could be also resolved by combining Eq. (37) and Eq. (39). As shown in Fig. 9, the typical stress-locking [32, 33, 34] could be clearly observed. This phenomenon sets the gradient-enhanced damage model apart from the phase-field model. While some subsequent researchers have suggested over-nonlocal enhancement models to address the issue of stress locking [45, 33], these models do not bridge the gap between the GED and phase-field models.

With the proposed method, the distribution of non-local variables within the regularization region can be solved accurately. Therefore, to prevent the damage from being confined to a single element, the element size should be selected in such a way that the regularization region should be made to span multiple elements to capture the spatial gradient of the non-local variable.

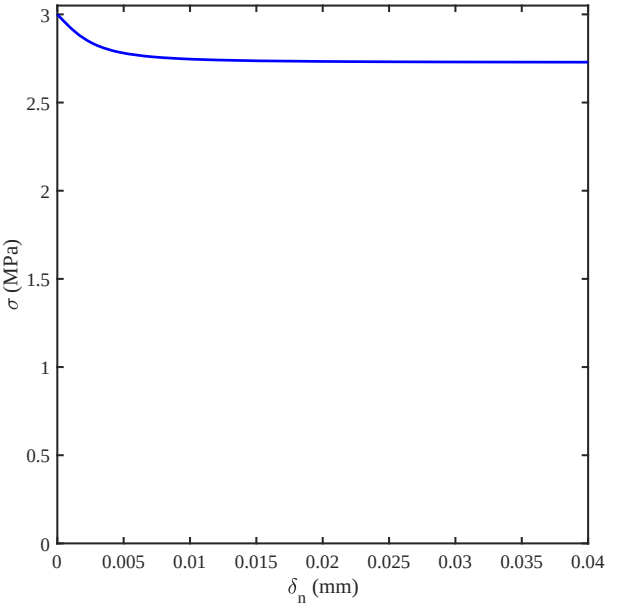

Figure 9: Cohesive law ($\delta_{\mathrm{n}} - \sigma$)

3. The thermodynamic framework of gradient-enhanced damage models

The fracture process in the real physical world is much more complex than described by Griffith's theory. Besides the energy dissipation occurring at the crack surfaces, other dissipative mechanisms also play a role within the fracture zone [46, 47]. These mechanisms may include friction, plastic deformation, damage evolution, and various other forms of energy dissipation. For such complex problems, the traditional principle of minimum potential energy is no longer applicable. Therefore, in this section, the thermodynamic framework of gradient-enhanced damage models is established based on the principle of energy conservation by considering additional dissipative forces. The energy functional containing dissipative forces within the framework of the gradient damage model can be expressed, taking the strain energy as a non-local variable, as follows:

$$\Pi = \int_{\mathcal{B}} \Psi_{\mathrm{crack}} \mathrm{d}V + \int_{\mathcal{B}} \Psi_{\mathrm{strain}} \mathrm{d}V + \Pi_{\mathrm{ext}} + \Pi_{\mathrm{diss}} \tag{40}$$

and

$$\begin{cases} \Psi_{\text{crack}} = \dfrac{l_c^2}{2}\left|\nabla\bar{Y}\right|^2 + \dfrac{1}{2}\bar{Y}^2 & \text{(41a)} \\ \Psi_{\text{strain}} = \left(1-\bar{\phi}\left(\bar{Y}\right)\right)\epsilon : \mathbb{E} : \epsilon & \text{(41b)} \\ \Pi_{\text{ext}} = -\displaystyle\int_{\mathcal{B}} \bar{\gamma}\cdot u \mathrm{d}V - \int_{\partial\mathcal{B}} \bar{t}\cdot u \mathrm{d}A & \text{(41c)} \\ \Pi_{\text{diss}} = \displaystyle\int_{\mathcal{B}} \mathrm{d}\mathcal{D}_{\text{diss}} & \text{(41d)} \end{cases}$$

where Ψ_{crack} is the crack density function, and Ψ_{strain} is strain energy density. Π_{ext} is the external potential energy. $\bar{\gamma}$ and $\bar{t}$ are bodily forces and boundary forces, respectively. Π_{diss} is the dissipative energy that generally can only be expressed in integral form. $\dot{\mathcal{D}}_{\text{diss}} = \int_{\mathcal{B}} f_{\text{diss}}\dot{\bar{Y}}\mathrm{d}V$, and f_{diss} is the dissipative force, $\dot{\bar{Y}}$ should be understood as the derivative of non-local variable $\bar{Y}$ with respect to some pseudo time.

As under the first law of thermodynamics, which is referred to as the law of conservation of energy,

$$\int_{\partial\mathcal{B}} \bar{t}\cdot\dot{u}\mathrm{d}A = \int_{\mathcal{B}} \left(\frac{\partial\Pi}{\partial\epsilon} : \dot{\epsilon} + \frac{\partial\Pi}{\partial\bar{Y}}\dot{\bar{Y}} + \frac{\partial\Pi}{\partial\nabla\bar{Y}}\nabla\dot{\bar{Y}}\right)\mathrm{d}V + \int_{\mathcal{B}} f_{\text{diss}}\dot{\bar{Y}}\mathrm{d}V \tag{42}$$

By employing partial integration followed by the application of the divergence theorem, Eq. (42) can be reformulated as follows:

$$\begin{aligned} &\int_{\mathcal{B}} \left[\mathcal{L}\left(\Psi_{\text{strain}}+\Psi_{\text{crack}}\right) + f_{\text{diss}}\right]\dot{\bar{Y}}\mathrm{d}V - \int_{\mathcal{B}} \nabla\cdot\frac{\partial\Psi_{\text{strain}}}{\partial\epsilon}\cdot\dot{u}\mathrm{d}V \\ =&\int_{\partial\mathcal{B}} \left(\bar{t} - n\cdot\frac{\partial\Psi_{\text{strain}}}{\partial\epsilon}\right)\cdot\dot{u}\mathrm{d}A - \int_{\partial\mathcal{B}} n\cdot\frac{\partial\Psi_{\text{crack}}}{\partial\nabla\bar{Y}}\dot{\bar{Y}}\mathrm{d}A \end{aligned} \tag{43}$$

where $\mathcal{L}(\cdot) = \partial(\cdot)/\partial\bar{Y} - \nabla\cdot\partial(\cdot)/\partial\nabla\bar{Y}$ is the Euler–Lagrange operator.

Since Eq. (43) is valid for all physically feasible combinations of $\dot{u}$ and $\dot{\bar{Y}}$, it follows that the governing equations and boundary conditions can be derived as follows:

$$\begin{cases} \nabla \cdot \sigma = 0, \quad \sigma = \dfrac{\partial \Psi_{\text{strain}}}{\partial \epsilon} & \text{(44a)} \\ \mathcal{L}\left(\Psi_{\text{strain}} + \Psi_{\text{crack}}\right) + f_{\text{diss}} = 0 & \text{(44b)} \end{cases}$$

and

$$\begin{cases} n \cdot \sigma = \bar{t} & \text{on } \partial\mathcal{B} \quad \text{(45a)} \\ n \cdot \dfrac{\partial \Psi_{\text{crack}}}{\partial \nabla \phi} = n \cdot \nabla \phi = 0 & \text{on } \partial\mathcal{B} \quad \text{(45b)} \end{cases}$$

In the framework of gradient-enhanced damage models, the form of dissipative forces is as follows:

$$f_{\text{diss}} = \left[\frac{\mathrm{d}\bar{\phi}\left(\bar{Y}\right)}{\mathrm{d}\bar{Y}} - \frac{1}{2}\right] \epsilon : \mathbb{E} : \epsilon \tag{46}$$

Substituting Eqs. (41a), (41b), and (46) into Eq. (44b) yields the governing equations for the nonlocal variables,

$$\mathcal{L}\left(\Psi_{\text{strain}} + \Psi_{\text{crack}}\right) + f_{\text{diss}} = 0 \Rightarrow l_{\text{c}}^2 \nabla^2 \bar{Y} - \bar{Y} + Y = 0 \tag{47}$$

Substituting Eq. (3a) into Eq. (46) yields an explicit expression for f_{diss}:

$$f_{\text{diss}} = \left[\frac{f_{\text{t}} e^{\alpha}}{\sqrt{2E_0}} \frac{1}{2\bar{Y}} e^{-\alpha\sqrt{\frac{2}{f_{\text{t}}\varepsilon_{\text{c}}}}\sqrt{\bar{Y}}} \left(\frac{1}{\sqrt{\bar{Y}}} + \alpha\sqrt{\frac{2}{f_{\text{t}}\varepsilon_{\text{c}}}}\right) - \frac{1}{2}\right] \epsilon : \mathbb{E} : \epsilon \tag{48}$$

The second law of thermodynamics states that the external power must be equal to or greater than the rate of increase of free energy, i.e.,

$$\int_{\partial\mathcal{B}} \bar{t}\cdot\dot{u}\mathrm{d}A \geq \int_{\mathcal{B}} \left(\frac{\partial \Pi}{\partial \epsilon} : \dot{\epsilon} + \frac{\partial \Pi}{\partial \bar{Y}}\dot{\bar{Y}} + \frac{\partial \Pi}{\partial \nabla \bar{Y}}\nabla\dot{\bar{Y}} \right) \mathrm{d}V \tag{49}$$

By substituting Equation (49) into Equation (42), one obtains:

$$\int_{\mathcal{B}} f_{\mathrm{diss}}\dot{\bar{Y}}\mathrm{d}V \geq 0 \Rightarrow f_{\mathrm{diss}} \geq 0 \tag{50}$$

A simple but tedious mathematical calculation of Eq. (48) shows that $f_{\mathrm{diss}} \geq 0$ is strictly satisfied at the initial stage of damage evolution. When the damage increases to a certain value, Eq. (50) no longer stands, and therefore the laws of thermodynamics are no longer satisfied. This is consistent with the conclusions obtained in Section 2. In the damage profiles obtained analytically (Fig. 3, Fig. 6, Fig. 8), the damage would unload at the edge of the regularization region after a certain stage of development, which does not satisfy the thermodynamic law.

It is worth noting that in damage mechanics theory, the softening function $\bar{\phi}\left(\bar{Y}\right)$ has the property that $\lim_{\bar{Y}\to\infty} \mathrm{d}\bar{\phi}\left(\bar{Y}\right)/\mathrm{d}\bar{Y} = 0$. Therefore, regardless of the softening function or cohesive law chosen, the GED model would experience negative energy dissipation after a certain level of damage development, which is an inherent flaw of the GED model.

4. Non-local model considering shear failure

In practical scenarios, the failure of engineering structures often results from the combined impact of various stress factors. It is inadequate to solely consider tensile stresses, as neglecting the influence of shear stresses can lead to disastrous consequences [48, 49]. When dealing with

solids experiencing complex stress conditions, it becomes imperative to account for the interaction between tension and shear to understand potential crack surfaces and damage mechanisms.

The task of identifying potential crack surfaces is difficult, and previous researchers have used a variety of methods. Freddi and Royer-Carfagni [50] utilized structural strain; Wu et al. [51] employed tensile-compressive decomposition; Feng and Li [22] adopted an energy multiscale approach; and Xue et al. [52] applied shear-tensile decomposition. In the context of cohesive fracture theory and its mixed failure mode [22], the tensile-shear stress state at the crack surface is shown in Fig. 10.

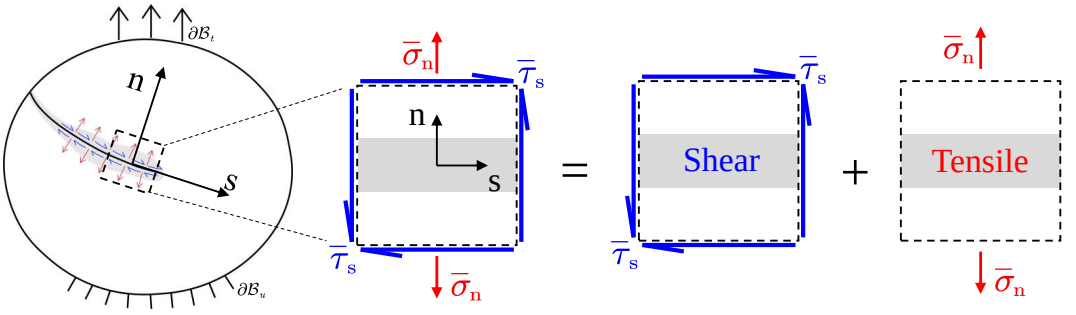

Figure 10: Tensile-shear stress state at the crack surface

Observing Fig. 10 reveals that the effective stress $\bar{\sigma}$ can be decomposed into $\bar{\tau}_{\mathrm{s}}$, representing the shear stress state, and $\bar{\sigma}_{\mathrm{n}}$, representing the tensile stress state. According to the tensile-shear stress state in Fig. 10, the strain energy Y can be expressed as:

$$Y = \frac{1}{2}\varepsilon : \mathbb{E} : \varepsilon = \frac{1}{2E_0}\left[2\left(1+\nu\right)\bar{\tau}_{\mathrm{s}}^2 + \bar{\sigma}_{\mathrm{n}}^2\right] = \frac{\bar{\sigma}_{\mathrm{n}}^2}{2E_0} + \frac{\bar{\tau}_{\mathrm{s}}^2}{2G_0} \tag{51}$$

and

$$\begin{cases} \bar{\sigma}_{\mathrm{n}} = \bar{\sigma}_{\max} + \bar{\sigma}_{\min} & \text{(52a)} \\ \bar{\tau}_{\mathrm{s}} = \sqrt{-\bar{\sigma}_{\max}\bar{\sigma}_{\min}} & \text{(52b)} \end{cases}$$

where ν is the Poisson's ratio, and G_0 is the shear modulus. $\bar{\sigma}_{\max}$ is the positive maximum principal stress, and $\bar{\sigma}_{\min}$ is the negative minimum principal stress.

Notice that the strain energy in Eq. (51) is only applicable to the tensile-shear stress state. In order to apply this to more complex stress states and to consider the tensile-compressive asymmetry [25] of quasi-brittle materials, this paper suggests the use of the damage energy release rate [4, 52] as the damage driving force.

$$Y = \sqrt{E_0 \mathbb{P}^+ : \bar{\sigma} : \mathbb{C} : \bar{\sigma}} \tag{53}$$

with

$$\begin{cases} \mathbb{P}^+ = \sum_i H\left(\hat{\bar{\sigma}}_i\right)\left(p_{ii} \otimes p_{ii}\right) & \text{(54a)} \\ p_{ij} = p_{ji} = \dfrac{1}{2}\left(n_i \otimes n_j + n_j \otimes n_i\right) & \text{(54b)} \end{cases}$$

where $\mathbb{C}$ is the fourth-order flexibility tensor. $\bar{\sigma} = \mathbb{E} : \varepsilon$, is the effective stress tensor. $\hat{\bar{\sigma}}_i$ is the i-th principal stress. n_i is the i-th normalized eigenvector corresponding to $\hat{\bar{\sigma}}_i$. $H(\cdot)$ is the Heaviside function.

In the GED model, every approach commences with a local variable Y, which undergoes transformation into a nonlocal variable $\bar{Y}$ through a Helmholtz-type partial differential equation. This study selects damage energy release rate as the non-local variable $\bar{Y}$, thus resulting in the non-local differential equation taking the following form:

$$\begin{cases} l_c^2 \nabla^2 \bar{Y} - \bar{Y} + Y = 0 \quad \text{on} \quad \mathcal{B} & \text{(55a)} \\ \nabla \bar{Y} \cdot n = 0 \quad \text{on} \quad \partial\mathcal{B} & \text{(55b)} \end{cases}$$

Inspired by Mazars [53], this work defines an energy ratio, θ, as the weights of tensile and shear damage in the assessment of the global damage of the material.

$$\theta = \begin{cases} 1 - \frac{\bar{\tau}_s^2 E_0}{\langle \bar{\sigma}_n \rangle^2 G_0 + \bar{\tau}_s^2 E_0} H\left(\bar{\sigma}_n\right) & \bar{\sigma}_{max} > 0 \text{ and } \bar{\sigma}_{min} < 0 \\ 0 & \text{Otherwise} \end{cases} \tag{56}$$

where symbols $< x >$ are the McAuley brackets (ramp function) defined as $\langle x \rangle = (x + |x|)/2$.

Then the damage to a material can be composed of tensile and shear damage.

$$\phi = \theta \phi_t + (1 - \theta) \phi_s \tag{57}$$

and

$$\begin{cases} \phi_t = 1 - \dfrac{f_t}{E_0 \sqrt{\frac{2\bar{Y}}{E_0}}} e^{\alpha_t \left(1 - \frac{\sqrt{\frac{2\bar{Y}}{E_0}}}{\varepsilon_c}\right)} & \bar{Y} \geq \dfrac{f_t^2}{2E_0} \quad (58a) \\ \phi_s = 1 - \dfrac{f_s}{G_0 \sqrt{\frac{2\bar{Y}}{G_0}}} e^{\alpha_s \left(1 - \frac{\sqrt{\frac{2\bar{Y}}{G_0}}}{\varepsilon_s}\right)} & \bar{Y} \geq \dfrac{f_s^2}{2G_0} \quad (58b) \\ \phi_t = 0; \phi_s = 0; & \text{Otherwise} \quad (58c) \end{cases}$$

where f_s is the shear strength. α_t and α_s are material softening parameters, $\varepsilon_c = \frac{f_t}{E_0}$, $\varepsilon_s = \frac{f_s}{G_0}$.

5. Numerical validations

The GED models are effectively solved through the application of the multi-field finite element method. When modeled with plane elements, each element node is characterized by three degrees of freedom (DOFs): two for the displacement field $\boldsymbol{u}$ and one for the non-local variable. The discretization process can be accomplished using either triangular linear elements or quadrilateral bilinear elements. In this study, we have successfully implemented numerical simulations using the FEniCS open-source finite element simulation package [54] and the ABAQUS user-defined element (UEL) of the subroutine [28]. In Section 5.1, FEniCS was employed to validate the

correctness of the analytical solution presented in Section 2. In the remaining examples, ABAQUS user-defined elements (UEL) were utilized for predicting crack extension, with the corresponding damage governing equations provided in Eqs. (55) and (57). In all numerical examples, the small deformation assumption is used, geometric nonlinearities are not considered, and plane stress elements are adopted.

5.1. Mode-I failure in a uniaxial tension of a 1D bar

Let us consider a rod of length $L = 100$ mm with a width of 5 mm. As shown in Fig. 11, the bar's left edge is fixed, while the right edge is stretched by applying the monotonically increasing displacement u^*. If not otherwise specified, the material parameters are chosen as follows: tensile strength $f_t = 3$MPa, Young's modulus $E_0 = 30$GPa and Poisson's ratio $\nu = 0$, characteristic length $l_c = 2$mm, softening parameters for exponential softening $\alpha = 0.1$, ultimate strain for linear softening $\varepsilon_u = 10 f_t / E_0$, the mesh size is 0.25 mm. The numerical prediction results involve the damage profile and cohesive law. Please note that a reasonable Poisson effect ($\nu < 0.5$) does not influence the comparison with the analytical solution. The use of $\nu = 0$ here is to minimize the effect of numerical error on the predictions, but $\nu = 0$ is not necessary. This study did not consider plastic strain, which is perfectly elastic after unloading, so this test was not considered for the unloading study.

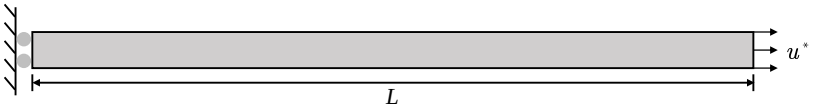

Figure 11: Uniaxial traction of a softening bar: boundary conditions

In this subsection, we have selected strain energy $\bar{Y}$, equivalent strain $\bar{\varepsilon}$, and damage $\bar{\phi}$ as non-local variables, respectively. We explore the behavior of the Gradient Enhanced Damage (GED) model by analyzing its non-local variable profiles, as depicted in Fig. 12. We find that the numerical predictions align well with the results obtained from mathematical analysis, validating the model's consistency under specific conditions.

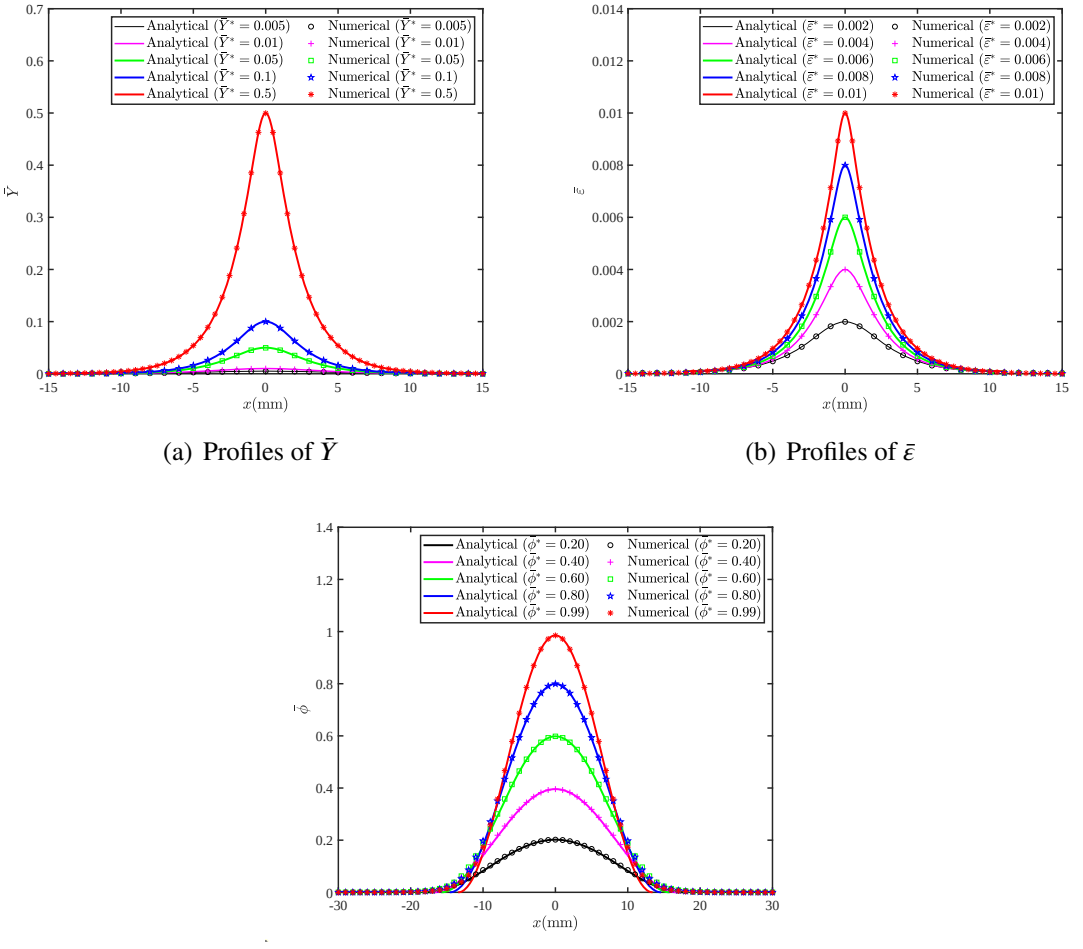

(a) Profiles of $\bar{Y}$

(b) Profiles of $\bar{\varepsilon}$

(c) Profiles of $\bar{\phi}$

Figure 12: Profiles of non-local variables (Analytical vs Numerical)

Fig. 13 illustrates the cohesive law of the GED model. The numerical predictions obtained are consistent with the results derived from mathematical analysis, indicating the reliability of the proposed approach. In particular, Fig. 13(c) visually explain stress locking in the GED model. These figures help us understand the phenomenon of stress locking more intuitively.

In traditional local damage models, the mesh size can have an influence on the prediction results. However, the GED model regularizes cracks in solids to a certain zone of damage distribution where the damage band spans multiple elements, so the mesh size does not affect the prediction. The predicted results of load versus displacement are given in Fig. 14 for characteristic length $l_c = 4$mm, mesh size $h = 0.25$mm, and mesh size $h = 0.125$mm. It is worth noting that in gradient

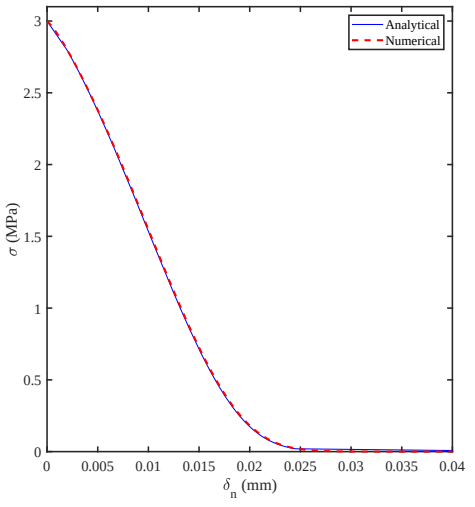

(a) Cohesive law ($\bar{Y}$)

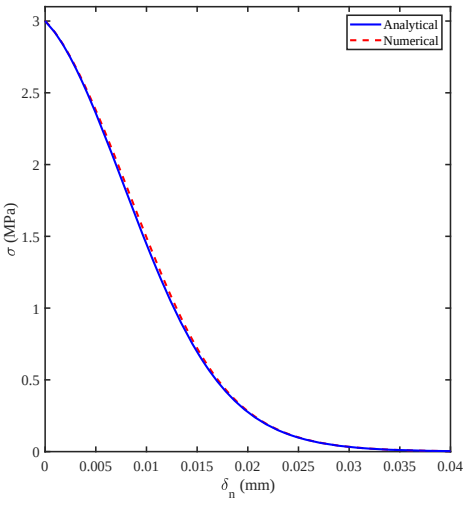

(b) Cohesive law ($\bar{\varepsilon}$)

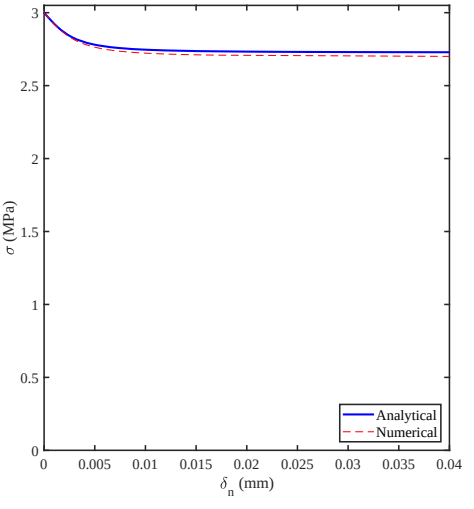

(c) Cohesive law ($\bar{\phi}$)

Figure 13: Cohesive law of non-local variables (Analytical vs Numerical)

damage, it is necessary for the damage bands to span a sufficient number of elements to capture the spatial gradients of the non-local variables to ensure that the computational results do not depend on the mesh size.

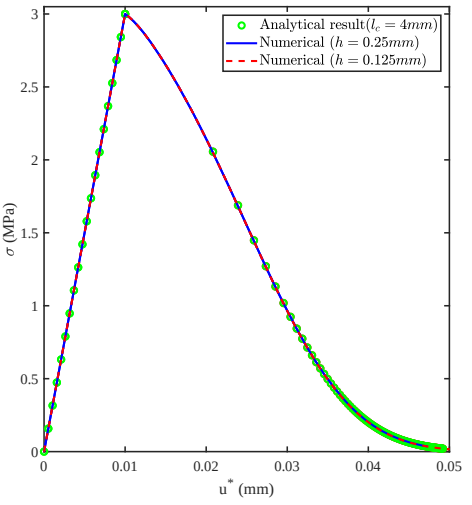

(a) load versus displacement ($\bar{Y}$)

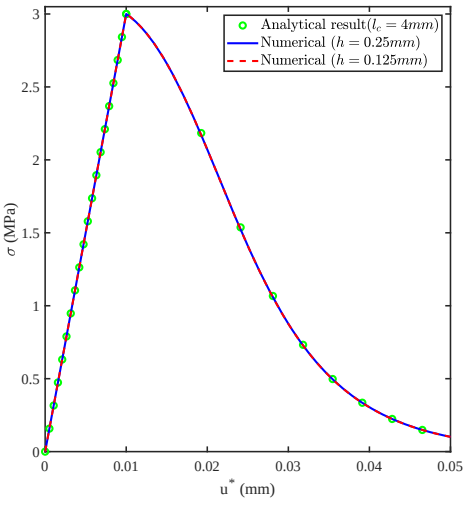

(b) load versus displacement ($\bar{\varepsilon}$)

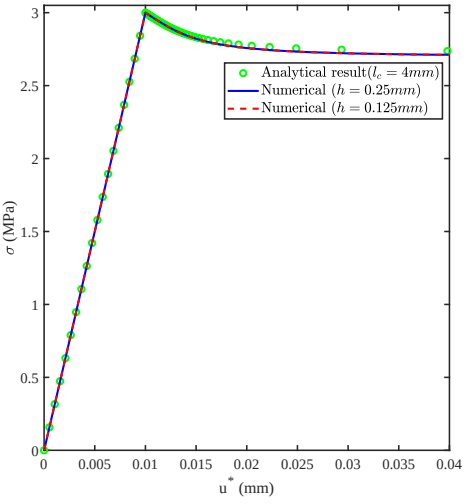

(c) load versus displacement ($\bar{\phi}$)

Figure 14: Comparison of predicted results for different mesh sizes

5.2. Three-point bending beam

In non-local damage models, the material characteristic length parameter is generally considered to influence the predicted results. Therefore, in this paper, a three-point bending beam [55] with Mode-I failure was selected. Three different internal lengths, i.e., l_c=1.0 mm, l_c=2.0 mm and l_c=3.0 mm, respectively, are considered in the numerical simulation. The material parameters are

as follows: Young's modulus $E_0 = 20\text{GPa}$, tensile strength $f_t = 2.2\text{MPa}$, Softening parameter $\alpha_t = 0.041$. Additionally, to alleviate the sensitivity to characteristic length, we utilize Eqs. (13) and (15) to compute the corresponding values of α_t for $l_c = 1\text{mm}$, 2mm, and 3mm when the tensile fracture energy $G_I = 0.097\text{N/mm}$. The calculated values for α_t are 0.0142, 0.028, and 0.041, respectively. It should be noted that this example belongs to Mode I fracture, and the alterations in the shear parameters have a little effect on the results.

The specimen's geometry, loading, and boundary conditions are shown in Fig. 15. Mode-I failure of the beam is caused by a crack appearing at the tip of the notch and propagating vertically along the line of symmetry. As depicted in Fig. 16, rather fine elements with the mesh size fixed as 0.25 mm are used around the centroid of the beam, and the mesh size at the ends of the beams are 10mm.

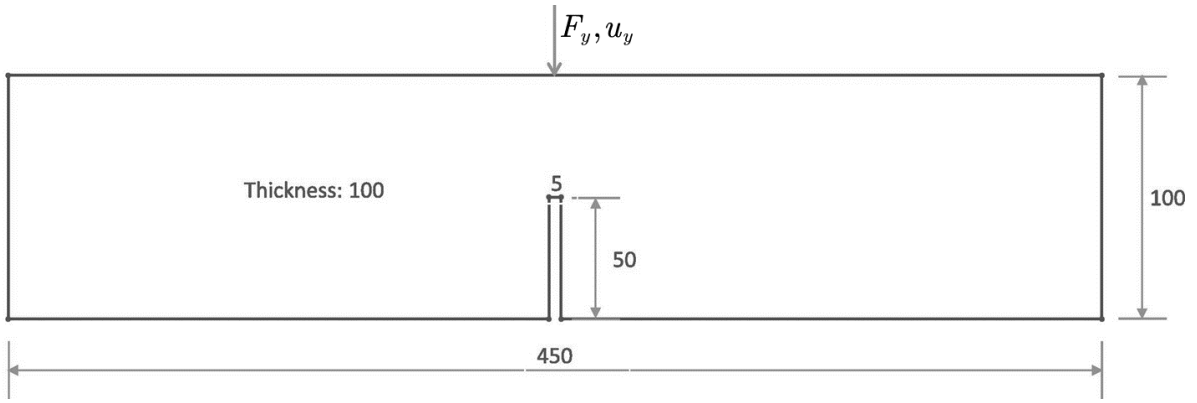

Figure 15: Notched concrete beam under three-point bending: Geometry (unit: mm), boundary conditions and loading

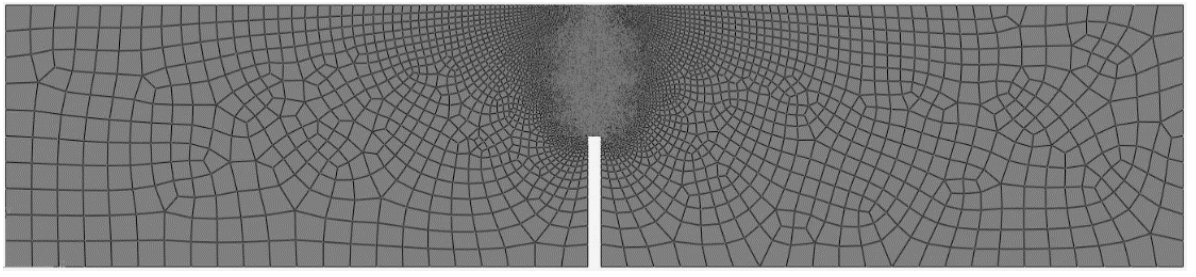

Figure 16: Notched concrete beam under three-point bending: 2D finite element mesh

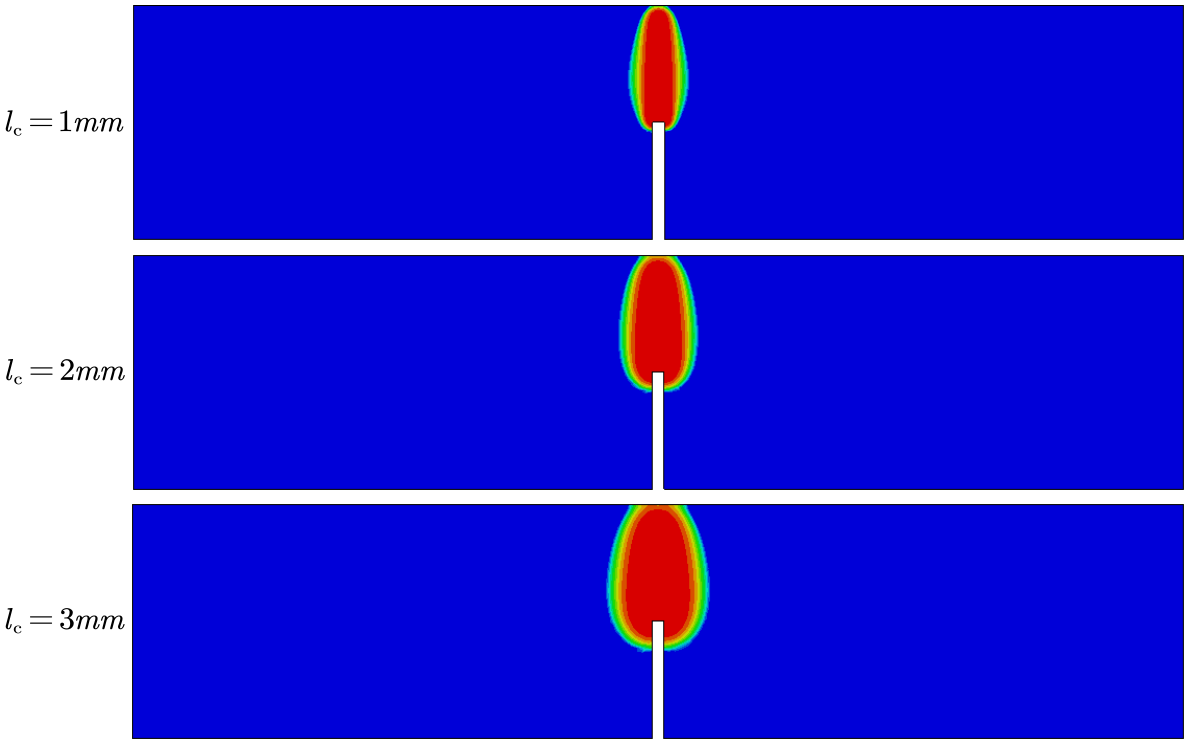

Figure 17: Notched concrete beam under three-point bending: Numerical prediction of ϕ

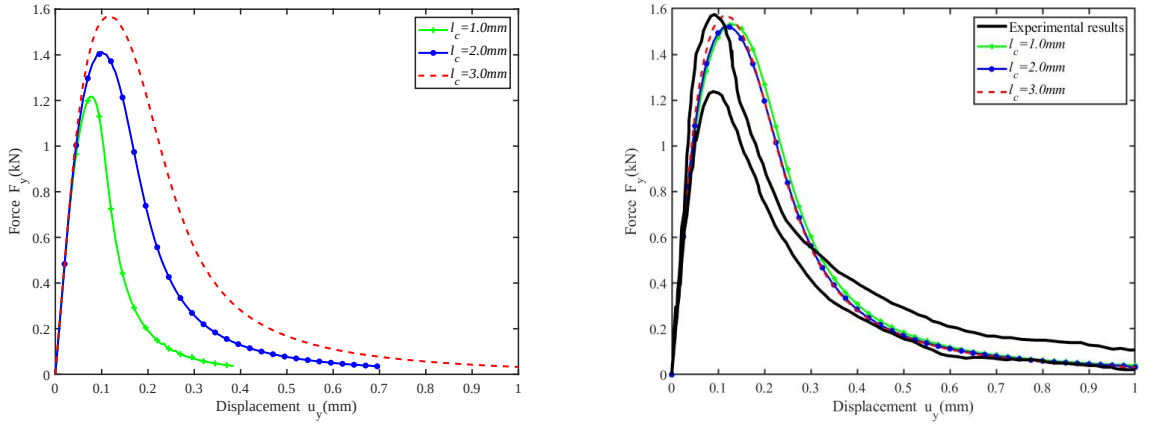

(a) Not calibrated for material parameter ($\alpha = 0.1$) (b) Calibration of material parameter by cohesive law

Figure 18: Notched concrete beam under three-point bending: Load versus displacement curves

In predicting the crack path (Fig. 17), the crack nucleates at the tip of the notch and propagates upwards to the top of the beam. As the characteristic length increases, the bandwidth of damage also increases. Upon examination of the force versus displacement curves (Fig. 18(a)), it is evident that

the GED model exhibits significant characteristic length sensitivity when the material softening parameter is not adjusted. This sensitivity also impacts the convergence of numerical calculations. In contrast, as depicted in Fig. 18(b), adjusting the softening parameter with a constant fracture energy not only alleviates characteristic length sensitivity but also improves the robustness of the numerical calculations.

5.3. Mixed-mode failure of notched beam

Next, this paper predicts notched beam tests for more complex mixed-mode failure. As depicted in Fig. 19, the specimen is of dimensions $675 \times 150 \times 50\text{mm}^3$, with a vertical notch of size $2 \times 75 \times 50\text{mm}^3$ at the bottom center. The load F_y was applied under displacement control, and the crack mouth opening displacement (CMOD) was monitored.

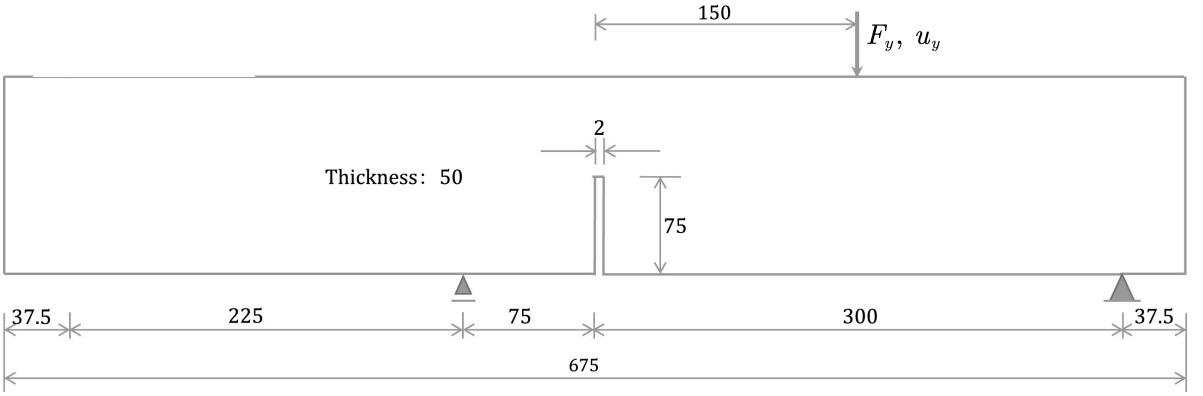

Figure 19: Mixed-mode failure of notched beam: Geometry (unit: mm), boundary conditions and loading

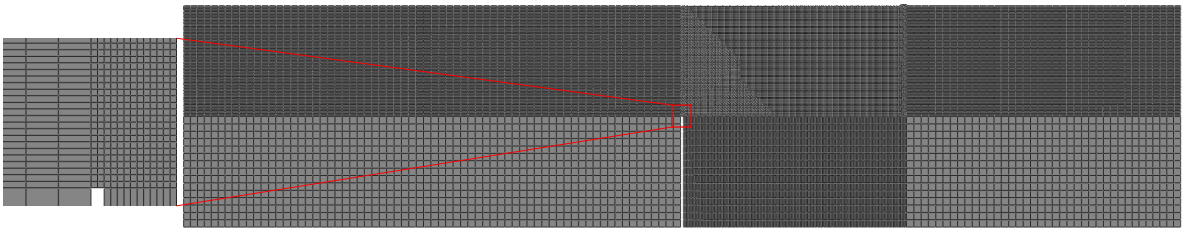

Figure 20: Mixed-mode failure of notched beam: 2D finite element mesh

Similar to Section (5.2), three different internal lengths are considered for this prediction: 1mm, 2mm, and 3mm. The material parameters are as follows: Young's modulus $E_0 = 38\text{GPa}$, tensile

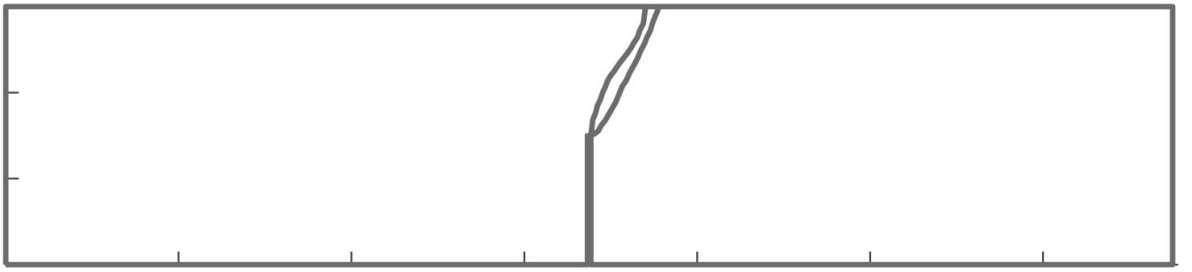

Figure 21: Mixed-mode failure of notched beam: Experimental crack

strength $f_t = 2.8$MPa, tensile fracture energy $G_I = 0.062$N/mm, shear strength $f_s = 3.0$MPa, and shear fracture energy $G_{II} = 0.155$N/mm. By the proposed approach in this paper, the tensile softening parameters α_t were calculated to be 0.018, 0.035, and 0.054 for different internal lengths, and the shear softening α_s was calculated to be 0.02, 0.039, and 0.059, respectively. The discretization of the computational domain is shown in Fig. 20. The size of the fine mesh in the model is 1 mm, and the size of the coarse mesh is 5mm.

The experimental cracks are shown in Fig. 21. The predicted results of the crack paths with different internal lengths are given in Fig. 22, and it can be clearly observed that the damage zone widens as the internal length increases. Good agreement between the predicted results and the experiment is achieved when the internal length takes a smaller value. The calculated curves of load versus crack mouth opening displacement are depicted in Fig. 23, where it can be seen that the effect of the internal length on the predicted results is significantly reduced after correction of the softening parameters by the proposed approach.

5.4. Double edge-notched specimens under non-proportional loading

This part presents numerical simulations of a challenging benchmark test [56] of concrete specimens with multiple (but not intersecting) cracks spreading simultaneously. This benchmark sample was chosen because it reflects several tests subjected to non-proportional loading conditions and showed curved cracks with different curvatures.

Fig. 24 depicts a plain concrete specimen with double-edge notches that measures $200 \times 200 \times 50\text{mm}^3$ and has two notches that are $25 \times 5 \times 50\text{mm}^3$ each in the middle of the left and right

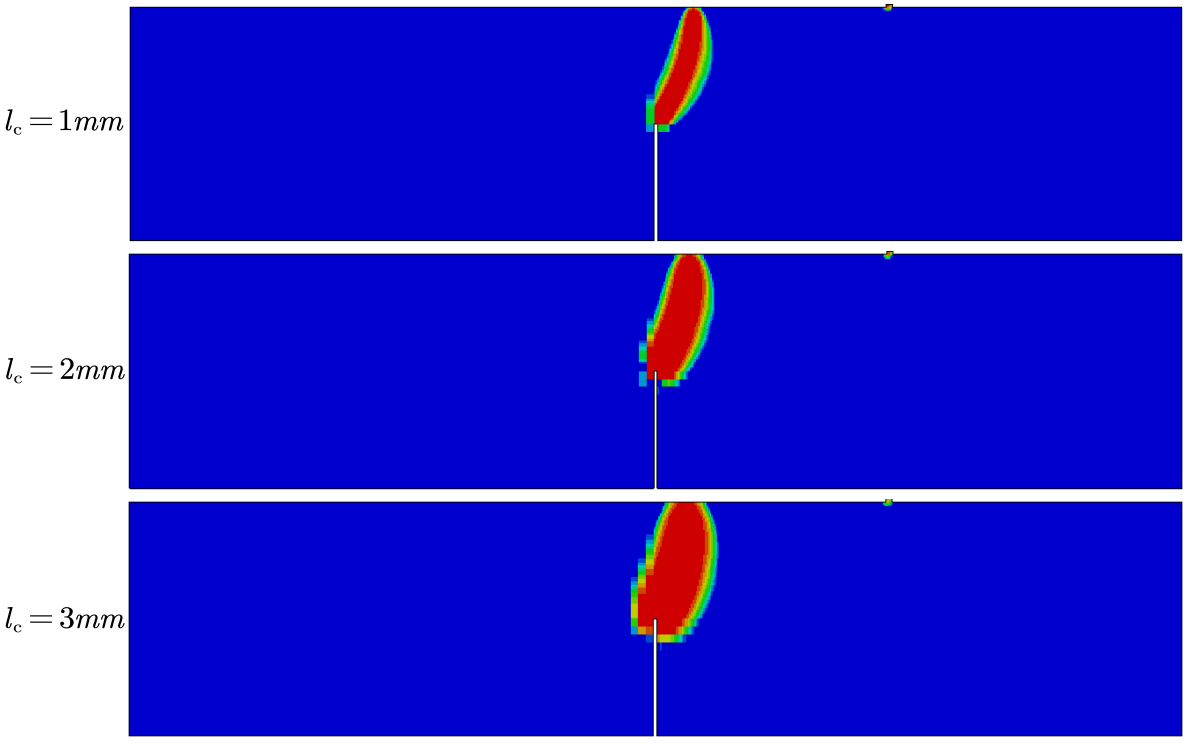

Figure 22: Mixed-mode failure of notched beam: Numerical prediction of ϕ

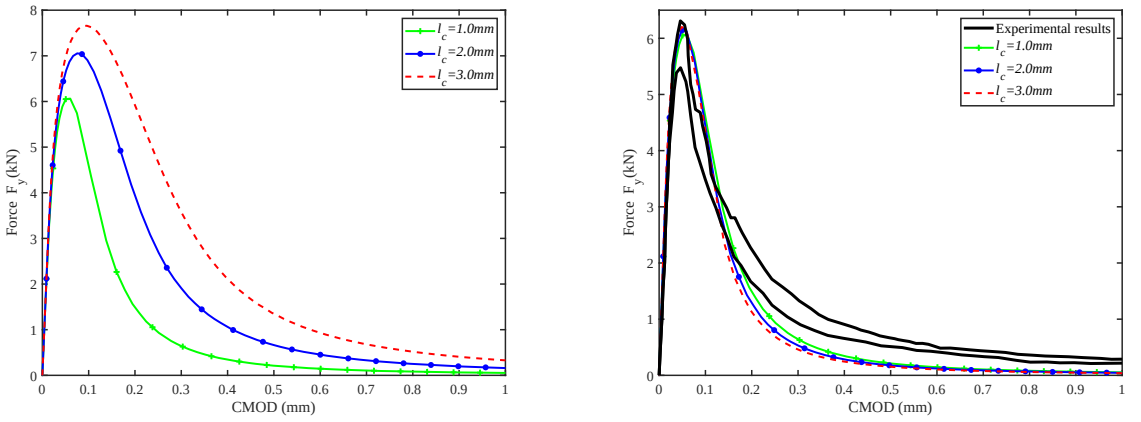

(a) Not calibrated for material parameter (b) Calibration of material parameter by cohesive law

Figure 23: Mixed-mode failure of notched beam: Load versus CMOD curves

sides. The specimen was glued to a unique, rigid steel frame, allowing for various loading paths that combine shear and tension while applying force or displacement control. The test loading is divided into two steps: the first step is the horizontal shear loading, and the second step is the

vertical displacement loading. More specifically, the horizontal shear force F_s was first applied along the left side above the notch. Then, keeping the horizontal shear force F_s constant, the vertical displacement u_y was applied to the top of the specimen while the corresponding vertical force F_y was recorded. Throughout the test, the specimen was supported at the bottom and right sides below the notch. In this work, the tests DENS-4a, DENS-4band, and DENS-4c are considered. They are different in the first-applied shear force: $F_s = 5kN$ for DENS-4a, $F_s = 10kN$ for DENS-4b, and $F_s = 27.5kN$ for DENS-4c, respectively. In this example, we have applied Q4 elements with a coarse mesh size of 5 mm and a locally refined mesh size of 1mm, as shown in Fig. 24.

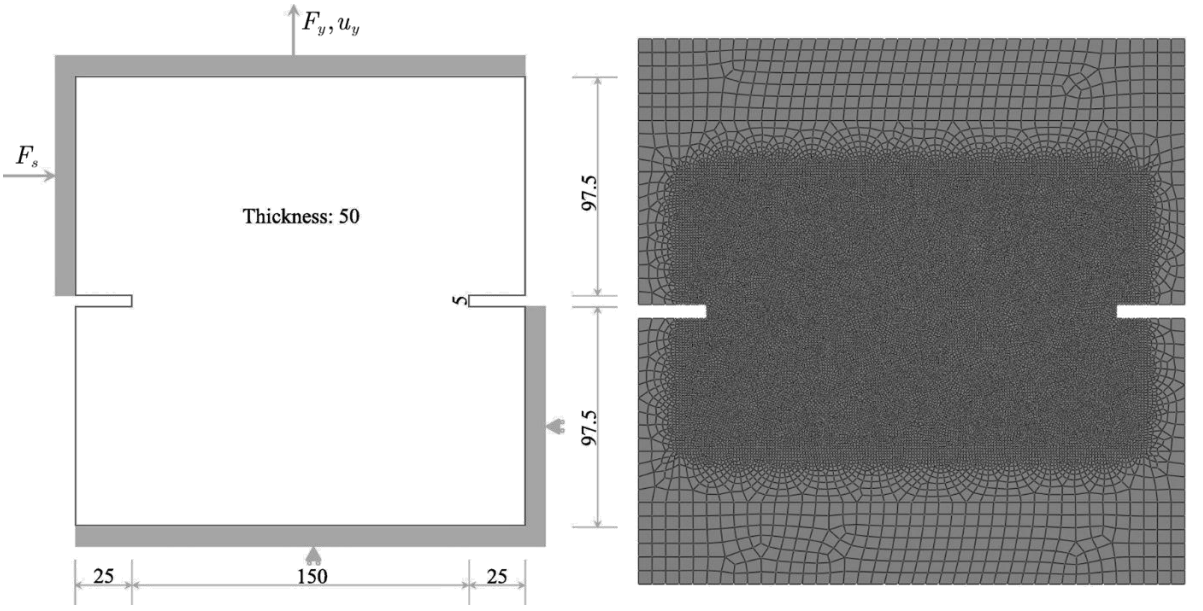

Figure 24: Double edge-notched concrete specimen: Geometry and boundary condition (left); and finite element mesh (right). Unit of length is mm.

Experimental findings show that two virtually antisymmetric cracks spread from the notches to the opposite sides and that the amount of the initial shear force F_s influences the curvature (Fig. 25). The tests provide ample evidence of concrete elements' different cracking paths and load-carrying capacity under different shear conditions. Appropriate material shear strength and shear failure mechanisms are required to predict this set of tests correctly. DENS-4a, DENS-4b, and DENS-4c specimens were simulated with the same material parameters in this subsection. The material parameters are as follows: Young's modulus $E_0 = 30$GPa, tensile strength $f_t = 2.4$MPa,

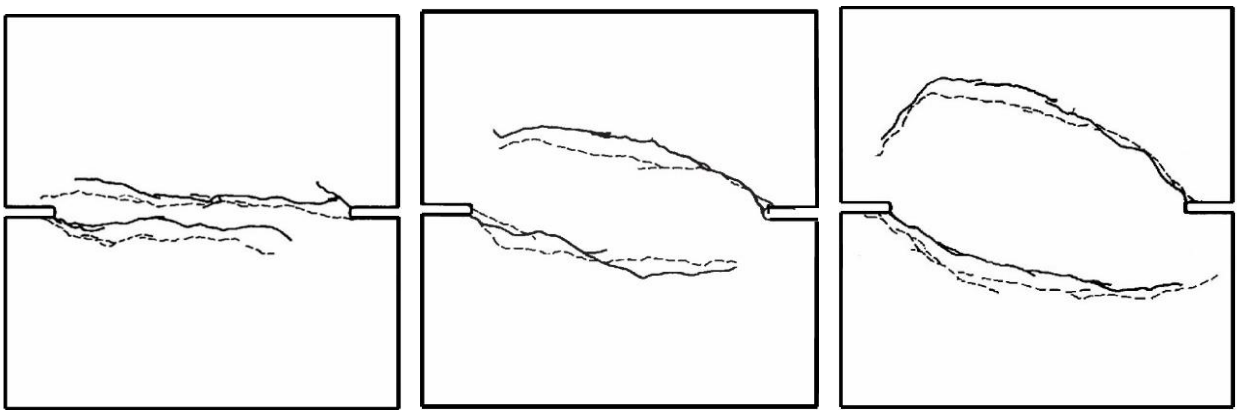

(a) DENS-4a (b) DENS-4b (c) DENS-4c

Figure 25: Double edge-notched concrete specimen: Experimentally observed cracks

tensile softening parameter $\alpha_t = 0.008$. shear strength $f_s = 4.0$MPa, shear softening parameter $\alpha_s = 0.006$, characteristic length $l_c = 0.32$mm.

Fig. 26 shows the numerically predicted crack development. The predictions match the experimentally observed crack paths very closely, with the curvature of the two antisymmetric cracks becoming greater as the first applied shear force F_s increases. Fig. 27 shows the predicted force-displacement curves. The peak force is overestimated in the numerical simulations of DEN-4b and DEN-4c, and this discrepancy has been observed in other numerical studies [47, 22, 57, 58]. Since this is not the goal of our study, we will not calibrate the parameters here to suit the experimental results. In Fig. 27(c), the load-displacement curves exhibit a large gap with the test results, and this gap is observed in numerous isotropic damage models. This gap can be attributed to the mismatched failure criteria. Specifically, under complex loading conditions, quasi-brittle materials exhibit significant damage-induced anisotropy, whereas in this paper, an isotropic damage model is adopted, which leads to a deviation from the actual results.

To ascertain whether the form of damage evolution influences the material's failure mode, we examined the crack paths of DEN-4a under the consideration of only tensile damage (i.e., $\phi = \phi_t$). As depicted in Fig. 28, the predicted cracks lead us to the conclusion that significantly inaccurate

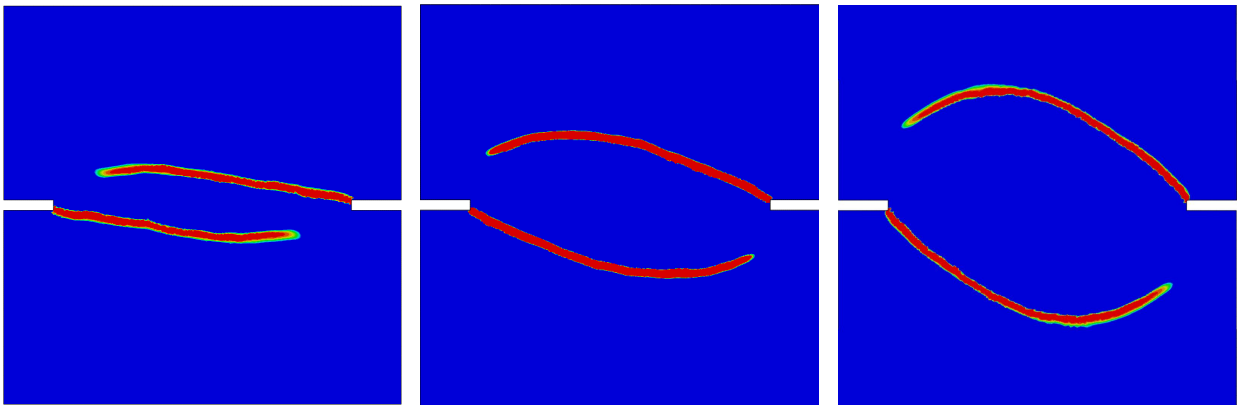

(a) DENS-4a (b) DENS-4b (c) DENS-4c

Figure 26: Double edge-notched concrete specimen: Numerical prediction of ϕ

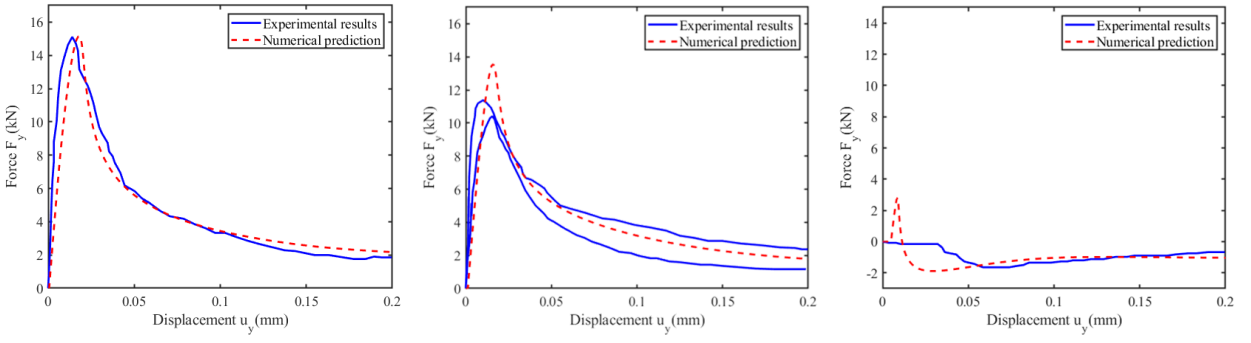

(a) DENS-4a (b) DENS-4b (c) DENS-4c

Figure 27: Double edge-notched concrete specimen: Load versus displacement curves

crack paths may be obtained if there is no differentiation between the shear and tensile damage evolution of the material.

6. Conclusion

This paper presents an approach to analytically solving the GED model, enabling the determination of damage profiles and cohesive laws. Through the theoretical solution, several key phenomena within the traditional GED model are validated, including damage widening, characteristic length sensitivity, and stress locking, elucidating the essential distinction between the GED model and the phase field model.

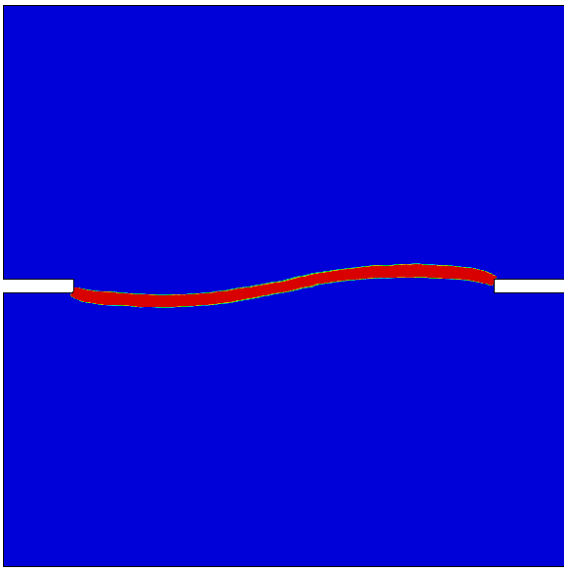

Figure 28: Double edge-notched concrete specimen: The predicted final crack paths by using $\phi = \phi_t$

449 The analytical solution of the cohesive law sheds light on the differences between the softening
450 law used in local damage models and the cohesive law required in the GED model. It highlights that
451 the softening law does not directly represent the cohesive behavior in the GED model. Furthermore,
452 establishing the fracture energy from the $\sigma - \delta_{\mathrm{n}}$ curve will assist in fine-tuning the model to
453 match and replicate the actual material properties. Numerical examples illustrate that adjusting
454 the softening parameter by fixing the fracture energy G_{I} effectively mitigates characteristic length
455 sensitivity. This implies that the analytical solution presented in this paper offers a feasible ap-
456 proach for calibrating parameters in GED models. Furthermore, the damage evolution formulation
457 proposed herein effectively captures failure behavior under complex stress. Currently, the proposed
458 gradient-enhanced damage model is limited only to infinitesimal deformations and quasi-static
459 failure. However, by employing an appropriate strain measure and the conjugate stress tensor, it
460 can effectively address geometric nonlinearities.

461 The findings presented in this paper significantly contribute to our understanding of gradient-
462 type damage models, providing valuable insights into their behaviour and properties. This analytical
463 framework opens up new avenues for future research and applications in the field of damage
464 modelling, enabling more accurate and comprehensive analyses of material damage and fracture

processes. However, unfortunately, neither the results obtained in this paper through the analytical solution improvement approach nor other empirical improvement approaches [59] are comparable to those predicted by the phase field model [25, 60], which can be attributed to the failure of the GED model to fully regularize the cracks. In Eqs. (5), (18), and (31), the relationship between local and non-local variables is established through the constitutive relation, but the establishment of this relationship lacks consideration of the cohesive law, so how to embed the cohesive law into the GED model will be an effective way to improve the GED model.

A. Finite element implementation

Using the Galerkin finite element method to discretize the model, the integral weak form of the gradient non-local Eq. (55a) and the stress balance Eq. (44a) can be expressed as:

$$\begin{cases} \int_{\mathcal{B}} \delta u \left(\nabla \cdot \sigma + \bar{\gamma}\right) \mathrm{d}V + \int_{\partial\mathcal{B}} \delta u \left(\sigma \cdot n - \bar{t}\right) \mathrm{d}A = 0 & \text{(A.1a)} \\ \int_{\mathcal{B}} \delta \bar{Y} \left(l_{\mathrm{c}}^2 \nabla^2 \bar{Y} - \bar{Y} + Y\right) \mathrm{d}V = 0 & \text{(A.1b)} \end{cases}$$

After mesh discretization, the displacement field u^h and the resulting strain field ϵ^h are interpolated in terms of the nodal displacements $a = \left\{ a_1 \quad \cdots \quad a_I \quad \cdots \right\}^T$.

$$\begin{cases} u\left(x\right) = \sum_I \mathrm{N}_{\mathrm{I}}\left(x\right) a_I = \mathrm{N}a & \text{(A.2a)} \\ \epsilon^h\left(x\right) = \sum_I \mathrm{B}_{\mathrm{I}}\left(x\right) a_I = \mathrm{B}a & \text{(A.2b)} \end{cases}$$

where in 2-D cases, the interpolation matrix $\mathrm{N} = \left\{ N_1 \quad \cdots \quad N_I \quad \cdots \right\}^T$ and the displacement-strain matrix $\mathrm{B} = \left\{ B_1 \quad \cdots \quad B_I \quad \cdots \right\}^T$ have the following components,

$$\mathrm{N}_I(x) = \begin{bmatrix} N_I(x) & 0 \\ 0 & N_I(x) \end{bmatrix}; \mathrm{B}_I(x) = \begin{bmatrix} lN_{I,x} & 0 \\ 0 & N_{I,y} \\ N_{I,y} & N_{I,x} \end{bmatrix} \tag{A.3}$$

for the interpolation function $N_I(x)$ associated to node I of the computational domain.

The non-local field $\bar{Y}(x)$ and its gradient $\nabla\bar{Y}(x)$ are also interpolated in terms of the nodal damage dofs $\bar{a} = \left\{ \bar{a}_1 \quad \cdots \quad \bar{a}_I \quad \cdots \right\}^T$.

$$\begin{cases} \bar{Y}(x) = \sum_I \bar{\mathrm{N}}_I(x)\,\bar{a}_I = \bar{\mathrm{N}}a & \text{(A.4a)} \\ \nabla\bar{Y}(x) = \sum_I \bar{\mathrm{B}}_I(x)\,\bar{a}_I = \bar{\mathrm{B}}a & \text{(A.4b)} \end{cases}$$

The interpolation function $\bar{N}_I(x)$ associated with the elements' node I in the localization band $\mathcal{B}$. Note that the displacement and damage fields are typically approximated using the same interpolation methods N_I.

Similar FE approximations for δu and $\delta\bar{Y}$ can be defined within the framework of the Bubnov-Galerkin method. It then follows from the governing equation in weak form Eq. (A.1) that,

$$\begin{cases} \delta a^T \left(\int_{\mathcal{B}} B^T \sigma \mathrm{d}V \right) = \delta a^T f^{\mathrm{ext}} & \text{(A.5a)} \\ \delta\bar{a}^T \left[\int_{\mathcal{B}} \bar{N}^T \left(-\bar{Y} + Y \right) - l_{\mathrm{c}}^2 \bar{B}^T \nabla\bar{Y} \mathrm{d}V \right] = 0 & \text{(A.5b)} \end{cases}$$

where f^{ext} is the standard external force vector.

The arbitrary nature of δa^T and $\delta\bar{a}^T$ produces the following semi-discrete equations in the residual form.

$$\begin{cases} r = f^{\text{ext}} - \int_{\mathcal{B}} B^T \sigma \mathrm{d}V & \text{(A.6a)} \\ \bar{r} = \int_{\mathcal{B}} \bar{N}^T \left(-\bar{Y} + Y\right) - l_{\text{c}}^2 \bar{B}^T \nabla \bar{Y} \mathrm{d}V = 0 & \text{(A.6b)} \end{cases}$$

The set of linear algebraic equations for the rectification of the nodal unknowns in the Newton-Raphson method is denoted by

$$\begin{bmatrix} K_{aa} & K_{a\bar{a}} \\ K_{\bar{a}a} & K_{\bar{a}\bar{a}} \end{bmatrix} \begin{bmatrix} \delta a \\ \delta \bar{a} \end{bmatrix} = \begin{bmatrix} r \\ \bar{r} \end{bmatrix} \tag{A.7}$$

where the tangent matrices are given by

$$\begin{cases} K_{aa} = -\dfrac{\partial r}{\partial a} = \displaystyle\int_{\mathcal{B}} B^T \frac{\partial \sigma}{\partial \varepsilon} B \mathrm{d}V & \text{(A.8a)} \\ K_{a\bar{a}} = -\dfrac{\partial r}{\partial \bar{a}} = \displaystyle\int_{\mathcal{B}} B^T \frac{\partial \sigma}{\partial \bar{Y}} \bar{N} \mathrm{d}V & \text{(A.8b)} \\ K_{\bar{a}a} = -\dfrac{\partial \bar{r}}{\partial a} = \displaystyle\int_{\mathcal{B}} \bar{N}^T \frac{\partial \bar{Y}}{\partial \epsilon} B \mathrm{d}V & \text{(A.8c)} \\ K_{\bar{a}\bar{a}} = -\dfrac{\partial \bar{r}}{\partial \bar{a}} = l_{\text{c}}^2 \displaystyle\int_{\mathcal{B}} \left(-\bar{N}^T \bar{N} + \bar{B}^T \bar{B}\right) \mathrm{d}V & \text{(A.8d)} \end{cases}$$

Since the Modified Newton Algorithm improves the computational efficiency of strongly nonlinear [61] and strongly coupled multi-field problems [62]. Therefore, the modified Newton algorithm is adopted in this paper. Where tangent matrices ignore the inter-field coupling to remove the off-diagonal matrices, leading to

$$\tilde{K}^{(0)} = \begin{bmatrix} K_{aa} & 0 \\ 0 & K_{\bar{a}\bar{a}} \end{bmatrix} \tag{A.9}$$

In the UEL compiled in this paper, a linear quadrilateral plane stress element with a 4-point Gaussian integration is used.

References

[1] Jian-Ying Wu, Vinh Phu Nguyen, Chi Thanh Nguyen, Danas Sutula, Sina Sinaie, and Stéphane PA Bordas. Phase-field modeling of fracture, 2020.

[2] Jeeho Lee and Gregory L Fenves. Plastic-damage model for cyclic loading of concrete structures. *Journal of engineering mechanics*, 124(8): 892–900, 1998.

[3] Jacob Lubliner, Javier Oliver, Sergio Oller, and Eugenio Oñate. A plastic-damage model for concrete. *International Journal of solids and structures*, 25(3):299–326, 1989.

[4] Jian Ying Wu, Jie Li, and Rui Faria. An energy release rate-based plastic-damage model for concrete. *International journal of Solids and Structures*, 43(3-4):583–612, 2006.

[5] Zdeněk P Bažant. Instability, ductility, and size effect in strain-softening concrete. *Journal of the engineering mechanics division*, 102(2): 331–344, 1976.

[6] Zdeněk P Bažant and Ted B Belytschko. Wave propagation in a strain-softening bar: exact solution. *Journal of Engineering Mechanics*, 111 (3):381–389, 1985.

[7] Zdenek P Bazant, Ted B Belytschko, Ta-Peng Chang, et al. Continuum theory for strain-softening. *Journal of Engineering Mechanics*, 110 (12):1666–1692, 1984.

[8] Milan Jirasek. Nonlocal models for damage and fracture: comparison of approaches. *International Journal of Solids and Structures*, 35 (31-32):4133–4145, 1998.

[9] E Lorentz and S Andrieux. A variational formulation for nonlocal damage models. *International journal of plasticity*, 15(2):119–138, 1999.

[10] JUAN CARLOS Simo, JAVIER Oliver, and Francisco Armero. An analysis of strong discontinuities induced by strain-softening in rate-independent inelastic solids. *Computational mechanics*, 12(5):277–296, 1993.

[11] Milan Jirásek. Non-local damage mechanics with application to concrete. *Revue française de génie civil*, 8(5-6):683–707, 2004.

[12] Ron HJ Peerlings, René de Borst, WA Marcel Brekelmans, and JHP0882 de Vree. Gradient enhanced damage for quasi-brittle materials. *International Journal for numerical methods in engineering*, 39(19):3391–3403, 1996.

[13] Imadeddin Zreid and Michael Kaliske. A gradient enhanced plasticity–damage microplane model for concrete. *Computational Mechanics*, 62:1239–1257, 2018.

[14] Zdeněk P Bažant and Milan Jirásek. Nonlocal integral formulations of plasticity and damage: survey of progress. *Journal of engineering mechanics*, 128(11):1119–1149, 2002.

[15] Michel Frémond and Boumediene Nedjar. Damage, gradient of damage and principle of virtual power. *International journal of solids and structures*, 33(8):1083–1103, 1996.

[16] Kim Pham, Hanen Amor, Jean-Jacques Marigo, and Corrado Maurini. Gradient damage models and their use to approximate brittle fracture. *International Journal of Damage Mechanics*, 20(4):618–652, 2011.

[17] Gilles Pijaudier-Cabot and Zdeněk P Bažant. Nonlocal damage theory. *Journal of engineering mechanics*, 113(10):1512–1533, 1987.

[18] R De Borst and LJ Sluys. Localisation in a cosserat continuum under static and dynamic loading conditions. *Computer Methods in Applied Mechanics and Engineering*, 90(1-3):805–827, 1991.

[19] BJ Dimitrijevic and K Hackl. A regularization framework for damage–plasticity models via gradient enhancement of the free energy. *International Journal for Numerical Methods in Biomedical Engineering*, 27(8):1199–1210, 2011.

[20] Juan C Simo and JW0634 Ju. Strain-and stress-based continuum damage models—i. formulation. *International journal of solids and structures*, 23(7):821–840, 1987.

[21] Ye Feng, Jiadi Fan, and Jie Li. Endowing explicit cohesive laws to the phase-field fracture theory. *Journal of the Mechanics and Physics of Solids*, 152:104464, 2021.

[22] Ye Feng and Jie Li. A unified regularized variational cohesive fracture theory with directional energy decomposition. *International Journal of Engineering Science*, 182:103773, 2023.

[23] Francesco Freddi. Fracture energy in phase field models. *Mechanics Research Communications*, 96:29–36, 2019.

[24] Francesco Freddi and Gianni Royer-Carfagni. Phase-field slip-line theory of plasticity. *Journal of the Mechanics and Physics of Solids*, 94: 257–272, 2016.

[25] Jian-Ying Wu. A unified phase-field theory for the mechanics of damage and quasi-brittle failure. *Journal of the Mechanics and Physics of Solids*, 103:72–99, 2017.

[26] Jian-Ying Wu and Vinh Phu Nguyen. A length scale insensitive phase-field damage model for brittle fracture. *Journal of the Mechanics and Physics of Solids*, 119:20–42, 2018.

[27] Milan Jirásek and Simon Rolshoven. Comparison of integral-type nonlocal plasticity models for strain-softening materials. *International Journal of Engineering Science*, 41(13-14):1553–1602, 2003.

[28] G Abaqus. Abaqus 6.11. *Dassault Systemes Simulia Corporation, Providence, RI, USA*, page 3, 2011.

[29] George Z Voyiadjis and Navid Mozaffari. Nonlocal damage model using the phase field method: theory and applications. *International Journal of Solids and Structures*, 50(20-21):3136–3151, 2013.

[30] MGD Geers, R De Borst, WAM Brekelmans, and RHJ0938 Peerlings. Strain-based transient-gradient damage model for failure analyses. *Computer methods in applied mechanics and engineering*, 160(1-2):133–153, 1998.

[31] René de Borst and Clemens V Verhoosel. Gradient damage vs phase-field approaches for fracture: Similarities and differences. *Computer Methods in Applied Mechanics and Engineering*, 312:78–94, 2016.

[32] Zdeněk P Bažant and Giovanni Di Luzio. Nonlocal microplane model with strain-softening yield limits. *International Journal of Solids and Structures*, 41(24-25):7209–7240, 2004.

[33] Leong Hien Poh and Somsak Swaddiwudhipong. Over-nonlocal gradient enhanced plastic-damage model for concrete. *International Journal of Solids and Structures*, 46(25-26):4369–4378, 2009.

[34] Angelo Simone, Harm Askes, and Lambertus J Sluys. Incorrect initiation and propagation of failure in non-local and gradient-enhanced media. *International journal of solids and structures*, 41(2):351–363, 2004.

[35] Ron HJ Peerlings, René de Borst, WAM Brekelmans, and Marc GD Geers. Gradient-enhanced damage modelling of concrete fracture. *Mechanics of Cohesive-frictional Materials: An International Journal on Experiments, Modelling and Computation of Materials and Structures*, 3(4):323–342, 1998.

[36] Qiao Wang, Qiang Yue, Wei Zhou, YT Feng, and Xiaolin Chang. Modeling of both tensional-shear and compressive-shear fractures by a unified phase-field model. *Applied Mathematical Modelling*, 117:162–196, 2023.

[37] Lu Hai, Jie Li, and Peter Wriggers. Relationship between probabilistic characteristics of microscopic and macroscopic strength within the stochastic phase-field model. *Applied Mathematical Modelling*, 123:776–789, 2023.

[38] Francesco Vicentini, Pietro Carrara, and Laura De Lorenzis. Phase-field modeling of brittle fracture in heterogeneous bars. *European Journal of Mechanics-A/Solids*, 97:104826, 2023.

[39] Eric Lorentz. A nonlocal damage model for plain concrete consistent with cohesive fracture. *International Journal of Fracture*, 207(2): 123–159, 2017.

[40] Luca Bisconti, Paolo Maria Mariano, and Xanthippi Markenscoff. A model of isotropic damage with strain-gradient effects: existence and uniqueness of weak solutions for progressive damage processes. *Mathematics and Mechanics of Solids*, 24(9):2726–2741, 2019.

[41] Lixian Zhao and Hang Cheng. Global weak solutions to the 1d phase-field model with inhomogeneous elasticity. *Applied Mathematical Modelling*, 104:567–586, 2022.

[42] Jie Li and Xiaodan Ren. Stochastic damage model for concrete based on energy equivalent strain. *International Journal of Solids and Structures*, 46(11-12):2407–2419, 2009.

[43] Kim Pham and Jean-Jacques Marigo. From the onset of damage to rupture: construction of responses with damage localization for a general class of gradient damage models. *Continuum Mechanics and Thermodynamics*, 25:147–171, 2013.

[44] Pomhyang Chu and Kumchol Yun. Three criteria for ensuring computational accuracy in phase field modelling. *Engineering Fracture Mechanics*, 263:108289, 2022.

[45] Giovanni Di Luzio and Zdeněk P Bažant. Spectral analysis of localization in nonlocal and over-nonlocal materials with softening plasticity or damage. *International Journal of Solids and Structures*, 42(23):6071–6100, 2005.

[46] Ye Feng and Jie Li. Phase-field cohesive fracture theory: A unified framework for dissipative systems based on variational inequality of virtual works. *Journal of the Mechanics and Physics of Solids*, 159:104737, 2022.

[47] Ye Feng and Jie Li. Phase-field method with additional dissipation force for mixed-mode cohesive fracture. *Journal of the Mechanics and Physics of Solids*, 159:104693, 2022.

[48] H Stamenkovic. Inflection points as statical supports are responsible for structural failure of amc warehouse in shelby, ohio, 1955. *Matériaux et Construction*, 10:375–384, 1977.

[49] Bernt Jakobsen and Finn Rosendahl. The sleipner platform accident. *Structural Engineering International*, 4(3):190–193, 1994.

[50] Francesco Freddi and Gianni Royer-Carfagni. Regularized variational theories of fracture: a unified approach. *Journal of the Mechanics and Physics of Solids*, 58(8):1154–1174, 2010.

[51] Jian-Ying Wu, Vinh Phu Nguyen, Hao Zhou, and Yuli Huang. A variationally consistent phase-field anisotropic damage model for fracture. *Computer Methods in Applied Mechanics and Engineering*, 358:112629, 2020.

[52] Liang Xue, Xiaodan Ren, and Roberto Ballarini. Damage-plasticity modeling of shear failure in reinforced concrete structures. *Engineering Fracture Mechanics*, 290:109536, 2023.

[53] Jacky Mazars. A description of micro-and macroscale damage of concrete structures. *Engineering fracture mechanics*, 25(5-6):729–737, 1986.

[54] Martin Alnæs, Jan Blechta, Johan Hake, August Johansson, Benjamin Kehlet, Anders Logg, Chris Richardson, Johannes Ring, Marie E Rognes, and Garth N Wells. The fenics project version 1.5. *Archive of numerical software*, 3(100), 2015.

[55] Jan Gerrit Rots. Computational modeling of concrete fracture. *ph.d.thesis delft university of technology*, 1988.

[56] Mohamed Buhary Nooru-Mohamed. Mixed-mode fracture of concrete: An experimental approach. *Ph. D. Thesis*, 1992.

[57] Günther Meschke and Peter Dumstorff. Energy-based modeling of cohesive and cohesionless cracks via x-fem. *Computer methods in applied mechanics and engineering*, 196(21-24):2338–2357, 2007.

[58] Jian-Ying Wu and Yuli Huang. Comprehensive implementations of phase-field damage models in abaqus. *Theoretical and Applied Fracture Mechanics*, 106:102440, 2020.

[59] Leong Hien Poh and Gang Sun. Localizing gradient damage model with decreasing interactions. *International Journal for Numerical Methods in Engineering*, 110(6):503–522, 2017.

[60] Jian-Ying Wu. A geometrically regularized gradient-damage model with energetic equivalence. *Computer Methods in Applied Mechanics and Engineering*, 328:612–637, 2018.

[61] Xiaodan Ren and Jie Li. Two-level consistent secant operators for cyclic loading of structures. *Journal of Engineering Mechanics*, 144(8): 04018065, 2018.

[62] Jian-Ying Wu, Yuli Huang, and Vinh Phu Nguyen. On the bfgs monolithic algorithm for the unified phase field damage theory. *Computer Methods in Applied Mechanics and Engineering*, 360:112704, 2020.